

Wave Energy Converter Based On Helmholtz Mode

A THESIS SUBMITTED TO THE GRADUATE DIVISION OF THE
UNIVERSITY OF HAWAII AT MANOA IN PARTIAL
FULFILLMENT OF
THE REQUIRMENTS FOR THE DEGREE OF

MASTER OF SCIENCE
IN
MECHANICAL ENGINEERING

DECEMBER 2013

By

Yalda Saadat

Thesis Committee:

Reza Ghorbani (Chairperson)

Ian Robertson

Brian Bingham

Abstract

The present study examines a new means of wave energy conversion inspired by geological toilet bowls and blowholes in nature that are able to concentrate ocean wave energy in a basin. The intention of this project is to experimentally investigate the geometry of toilet bowls in a wave tank enclosing the size of the basin and the channel in order to attract Helmholtz resonance and introduce a new device that is called resonator. The device includes a basin with a horizontal cross-sectional area at the level of mean-water level A_0 connected to the incoming waves by a narrow channel of width B and Length L , where the maximum water depth is H . The geometry of the device that is scaled by Froude number, causes an oscillating fluid within the channel with a Helmholtz frequency of $\sigma^2 H = gHB/A_0 L$.

In this article, the relation of the aforementioned frequency to the device's geometry is examined in both $1/25^{\text{th}}$ and $1/7^{\text{th}}$ scaled models. Additionally, the effect of the device's length and the angle of the device's winglets at the inlet of the channel are explored. Lastly, in this article, the $1/25^{\text{th}}$ device is tested with a two-dimensional particle image velocimetry instrument (PIV) to determine the instantaneous velocity field through the scaled model.

The experiments demonstrate that reducing the winglets' angle results in less high order harmonics, therefore, higher performance of wave energy absorption. In addition, the alignment of the axis of the resonator to incoming waves plays an important role in increasing the efficiency of the device.

Moreover, the collected data determines that resonance in the channel results in an amplification of wave height and corresponding wave power absorption relative to incoming waves. Accordingly, the appropriate location for placing the power take-off (PTO) can be empirically determined. There are different operating points for power extraction at different mean velocity in the channel, in which, the efficiency of the PTO as well as the wave power ratio flux in the channel are changing. Therefore, PTO can be tuned to operate at optimum power point.

This thesis that is the beginning of my journey, is dedicated to all people in my country and in the world with the same abilities and desires as me, who would like to study and enjoy expressing themselves in academia, but, are banned from doing so because of their beliefs, their religions, their thoughts and their way of thinking.

ACKNOWLEDGEMENT

First and foremost, I have to thank my parents for their endless love, support and words of encouragement throughout my life. Thank you both for bearing this long distance and giving me the strength to chase my dreams. Special thanks to my love, Mehdi, who never left my side and his support, his love and his understanding, make everything that I do possible. My little brother Babak deserves my whole hearted thanks as well.

Also, I would like to thank my adviser professor Reza Ghorbani in a special way, thanks for your patience, support, guidance, for sharing knowledge, passion and motivation, for giving me independence in my research and daring to me express my ideas. I enjoyed every single moment of working with you. I would like to express my gratitude to my committee members as well. Professor Ian Robertson, whom it was a great honor to be his student. He is one of the heroes of my life. Professor Brian Bingham who I had the fortune to be his teaching assistant and I learned from him a lot while working with him; you are really great.

Professor Mehrdad Ghasemi Nejhad, Professor Beei-Huan Chao and Professor Roger Babcock, whom without support of them my dual Master degrees were not possible. Thank you because you are the best chair and graduate chairs that I have ever seen.

Additionally I have to express my appreciation to Nelson Fernandez and Alexie Samimi because all their helps during my experimental work and their assistance when I needed.

At the end, I would like to thank the Renewable Energy and Island Sustainability (REIS) program, which is funded in part by the US Department of Energy Grant, DE-OE0000394, because of financially support of this research.

Table of Contents

CHAPTER 1:	INTRODUCTION	9
1.1	Introduction	9
1.2	The advantages of wave energy as a resource.....	9
1.3	Challenges	10
1.4	Background	10
1.5	Motivation and Introducing a new device, named Resonator	16
CHAPTER 2:	GOVERNING EQUATIONS.....	18
2.1	Governing Equations.....	18
CHAPTER 3:	Experimental set up.....	23
3.1	1/25 th scale set-up	24
3.2	Analysis and results of 1/25 th scale device.....	30
3.3	1/7 th scale set-up	38
3.4	Analysis and results of 1/7 th scale device.....	40
CHAPTER 4:	PIV Experiment	45
4.1	Experimental Equipment.....	45
4.2	Experimental Equipment.....	46
4.3	Experimental Conditions.....	47
CHAPTER 5:	SUMMARY AND CONCLUSIONS	56
CHAPTER 6:	REFERENCES	58

List of Figures

Figure 1-1: Price wave power classification	14
Figure 1-2: Natural Resonator at Hanauma Bay, Hawaii.	17
Figure 2-1: Top view of a basin with narrow channel	18
Figure 3-1: A sketch of the proposed design.	25
Figure 3-2: A sketch of the top and side views of the experiment.	25
Figure 3-3: Location of the three wave gauges.....	26
Figure 3-4: Top view of the length and angle of winglets.....	29
Figure 3-5: Wave Gauge Sample Data	30
Figure 3-6: Sample of dominant frequency	31
Figure 3-7: Phase Angle of the Signal for Each Inherent Frequency.	32
Figure 3-8: Phase Shift of the three combinations of signals.	33
Figure 3-9: Theoretical and Experimental Comparison of Helmholtz Mode.	34
Figure 3-10: Results of the Second Experiment exploring the effects of channel reduction angles through the implementation of a range of winglets.	35
Figure 3-11: Third Experiment exploring the arbitrary implementation of a one-way gate and channel blockage to represent the resistance of flow posed by the use of a submerged turbine. (Flap)	36
Figure 3-12: Third Experiment exploring the arbitrary implementation of a one-way gate and channel blockage to represent the resistance of flow posed by the use of a submerged turbine. (40%)	36
Figure 3-13: Third Experiment exploring the arbitrary implementation of a one-way gate and channel blockage to represent the resistance of flow posed by the use of a submerged turbine. (60%)	37

Figure 3-14: Third Experiment exploring the arbitrary implementation of a one-way gate and channel blockage to represent the resistance of flow posed by the use of a submerged turbine. (80%)	37
Figure 3-15: The experimental device at 1/7th scale.	39
Figure 3-16: 1/7th scale model of the Resonator with response plot.....	40
Figure 3-17: Power ratios of basin wave heights to incoming wave heights for three angles of incidence, from top to bottom: 0°, 15°, and 30°	42
Figure 3-18: Power –Take off in the Resonator.....	44
Figure 4-1: PIV Experimental Setup.....	47
Figure 4-2: Top view and side view of device, the bottom figure is PIV image for T =1.5 Sec.....	49
Figure 4-3: Velocity vectors after 1/6 sec.....	50
Figure 4-4: Velocity vectors after 1/3 sec.....	50
Figure 4-5: Velocity vectors after 1/2 sec.....	51
Figure 4-6: Velocity vectors after 2/3 sec.....	51
Figure 4-7: Velocity vectors after 5/6 sec.....	52
Figure 4-8: Velocity vectors after 1 sec.....	52
Figure 4-9: Velocity vectors after 1 1/2 sec.	53
Figure 4-10: Velocity vectors after 1 1/3 sec.....	53
Figure 4-11: Average velocity in whole channel, maximum, and minimum particle velocity at each instantaneous time in the channel	54

List of Tables

Table 1-1: Classification according to power flow	13
Table 1-2: Power conversion chains for selected WECs	15
Table 3-1: Winglet Sizes used in the experiment and the corresponding angles.....	28
Table 3-2: Table of the Ratios of Gauge 3 to Gauge 1 and the respective winglet	28

CHAPTER 1: INTRODUCTION

1.1 Introduction

The goal in this research is introducing a new wave energy converter that is more efficient with low cost.

Ocean waves have until now remained relatively untapped. The ocean is widely considered to be a vastly available, inexhaustible, and nonpolluting resource, and the potential of extracting energy from the waves is significant. In order to combat the growing global energy crisis and all of its challenges—to tackle climate change and to reduce greenhouse gasses—the need to exploit alternative, reliable, and environmentally-friendly resources is pressing. This readily available and inexhaustible source of ambient energy has in recent decades garnered global attention in terms of extraction of wave energy and it is one of the most important research areas for renewable energy. Many scientists and engineers around the world are investing in renewable energy technologies. Unlike the established major renewable energy sources—wind, solar and hydro—wave energy remains comparatively unexploited, and thus we find ourselves at the exciting new frontier of wave energy. Wave energy is, in a sense, a form of solar energy that is highly concentrated. The temperature differences across the earth that are produced from the sun cause winds to blow over the ocean's surface, generating waves. The power potential of these waves is tremendous-- much higher in fact than wind or solar power. Energy that is captured from waves has the potential to make a considerable contribution to future energy provision.

1.2 The advantages of wave energy as a resource

Ocean waves contain the largest energy density amongst the available renewable energy sources, and waves are one of the resources that can be harnessed with minimal negative environmental impacts, aiding in the de-carbonization of the world's energy climate.

Waves can travel thousands of miles from their origin with little energy loss. These deep water waves function very differently from the waves that are seen breaking on the beach, and these two should not be confused with each other. When the waves reach a point where water depth is less than half their wave length, the speed decreases such that the wave length decrease as well, leading to breaking, which is where the greatest energy loss occurs. The quantity of energy carried by each wave is considerable, and is proportional to the wave's period, and to the square of its height. Both kinetic and gravitational potential contribute to the total energy of waves.

The large energy density of ocean waves is the strongest reason why wave energy has the potential to become such a great resource. The development of wave energy conversion technology will enable ocean waves to be commercially viable, contributing significantly to the global energy mix.

1.3 Challenges

To achieve the aforementioned goals, there are several challenges that researchers in this field must overcome. While there has been tremendous progress in the development of wave energy conversion technology, advancement in the efficiency and cost of wave energy devices must be made through further research and investment before wave energy can become a commercially feasible alternative.

The conversion of slow oscillatory motion that carries reasonable energy into useful mechanical motion that can generate electricity is at the heart of the challenge of developing wave energy device. The power levels of waves vary according to their height and period, and these inputs must to be converted into smooth electrical outputs, making the task of a wave energy conversion device apparent.

1.4 Background

The idea of converting wave energy to electricity has been overlooked in the past decades, In fact, one of the first references of a wave energy converter (WEC) comes

from France's Girard brothers, in 1799, however much of WEC theory was developed in the 1970's. Since the energy crisis of 1973, studies aimed at a better understanding of wave power in order to find a reliable and economical method to convert wave energy into electricity. There were many ideas for WEC devices and numerous interesting theories, which were well established. The pioneers include Masuda [1], Salter [2], Mei [3-5], Flans [6,7], Newman [8,9], Bubal [10], Evance [11,12], Fujita [13], and Drew [14]. Thus, diverse methods of wave energy extraction have arisen: Scotland's Pelamis Wave Energy Converter [15], Oyster [16], Sweden's Lysekil Project [17], Duck wave energy converter [18], Aqua Buoy [19], Limpet [20], Wave Dragon [21], and many other are notable designs.

After 1970's progress has been made in this area of research, a large variety of concepts have been developed. There are currently more than a thousand WEC designs. However, there is still a need for developing WEC devices that are much more efficient and economical with minimal environmental impacts.

Price has presented a short summary of WEC classification [22]. Classification according to location (shoreline, near shore or offshore) [23] was, and still is [24], a widely used system. The generation of development [24] is another form of classification that has been around for a long time and is a subjective view of the state of development. However, these forms of classification are not useful for comparing operating principles of WECs, they contain no information regarding the equation of motion and hence efficiency of a WEC concept. Thus, classification based on the mode of motion or functional decomposition may be effectively utilized to compare groups of WECs.

The need for information regarding types of required machinery and the types of engineering challenges has led to new form of classification based on sub-system or operational principles. The eldest method of WEC classification is French's functional decomposition, French considered four main functional categories [25]:

- 1- Working surface (a rigid solid, flexible solid or gas)
- 2- Means of reaction (fixed, such as to the seabed or shoreline; balancing; inertial)
- 3- Configuration (terminator; attenuator; point-absorber)

- 4- Means of power extraction (pneumatic; oil hydraulic; water hydraulic; direct electrical). According to Clément classification, WECs are classified based on operating principles and location [26].

Four main operating principles are:

- 1- Oscillating water columns
- 2-Wave activated bodies
- 3-Overtopping devices
- 4-Unclassifiable (for example the Clam flexible bag device).

Salter [26] made the method of classification based on sub-system more simple. He considered six main sub-systems such as:

- I. A slow primary displacement element (float; flap; water column).
- II. Means of reaction (fixed; water column inertia; device mass inertia; balancing).
- III. A connecting linkage, which transmits the required forces while avoiding forces, which would be damaging for the structure.
- IV. Power conditioning: velocity increase and direction rectification.
- V. Generation: a fast moving unidirectional rotating part, driving an electrical machine.
- VI. Transmission: cables, transformers and switchgear for transmitting power to shore.

Price suggested a new concept of WECs classification based on the flow of power as shown in table 1-1. This method clarifies the impact of the design on the equation of motion, and the control interactions. In her proposed method, several stages required to

convert the power of the wave to the final energy carrier, are considered. The Fig. 1-1 shows this procedure.

Table 1-1: Classification according to power flow

Options separated by commas are independent and any number may be selected; options separated by forward slashes are mutually exclusive and one must be selected. The ellipsis (. . .) indicates that other suitable options are possible.

Power transfer stage	Attributes	Options
Intercepted power	Type of primary/secondary interface modes of motion orientation location power conditioning	oscillator / pulsating solid / pulsating fluid heave, sway, surge, pitch, yaw, roll point absorber / terminator, attenuator shoreline / near shore, offshore none/gearing, rectification storage, limitation
Captured power	means of reaction energy carrier power conditioning	fixed / balancing / inertia electricity / fluid flow . . . none/gearing, rectification storage, limitation
Delivered Power	Energy carrier power conditioning	electricity / chemical . . . none/gearing, rectification storage, limitation

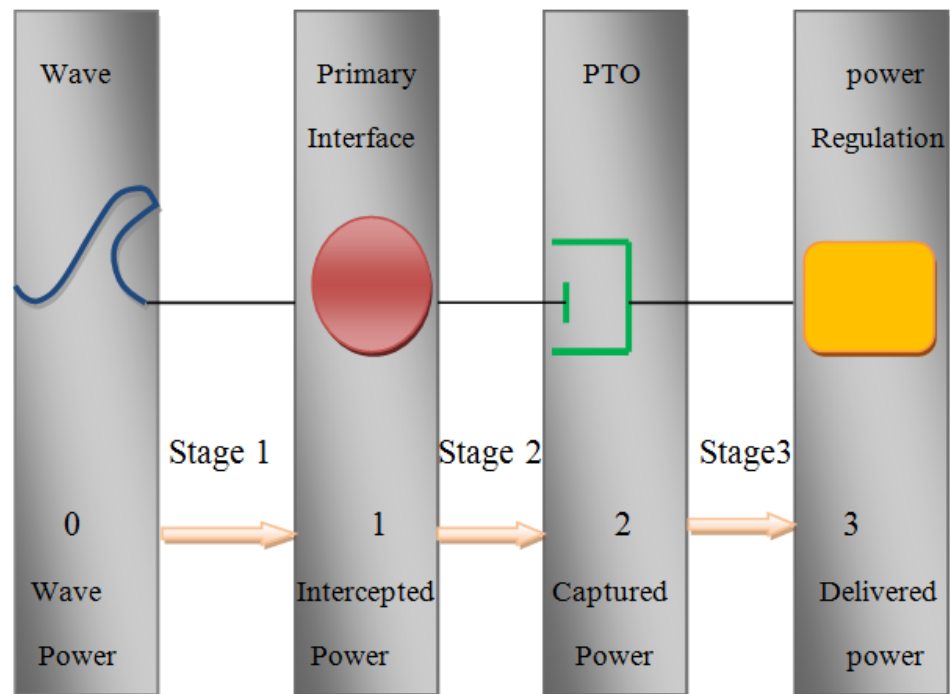


Figure 1-1: Price wave power classification

I. The flow of power between the wave (0) and the primary interface (1), gives the intercepted power. Primary interface is something that power carried by the wave converts to in the first step of power conversion. The primary interface determines how much of the power in the waves is modified into a more readily captured form. The second stage determines how much of this intercepted power is retained by the WEC (captured power) and how much is returned back to the sea (radiated power). Three types of primary interface exist, an oscillating solid, a pulsating solid and pulsating liquid.

II. The flow of power between the primary interface and the PTO (2), gives the captured power.

III. The flow of power between PTO and the final stage of power conversion (3), gives the delivered power.

In table 1-2 , Price showed how some selected wave energy converters work with her idea and we add the last row to her table to explain how our new device, Resonator that will be explained completely in the next chapter, takes advantages of her classification.

Table 1-2: Power conversion chains for selected WECs

WEC Concept	Examples	Stage 1	Stage 2	Stage 3
Oscillator with hydraulic transmission	Pelamis, Duck CETO, Oyster	oscillating solid oscillating solid	Hydraulic transmission – pulsating fluid: rectification, gearing, storage, pressurized seawater: rectification, gearing, storage	fluid machine high head hydro turbine
Oscillator with rotational transmission	Manchester bobber	oscillating solid	rotating shaft: gearing, storage (flywheel), ½, rectification	generator
Solid pulsator with hydraulic transmission	AWS 2008	pulsating solid - oscillating solid	Hydraulic transmission: gearing, storage, rectification	fluid machine
Solid pulsator with direct drive	AWS 2004	pulsating solid - oscillating solid	direct drive generator	power conditioning: gearing, smoothing
	Clam	pulsating solid - pulsating air	water turbine directly driven	power conditioning: gearing, smoothing
OWEC	Limpet; Azores OWC	pulsating water -pulsating air	oscillating air column: gearing	Air turbine: rectification
Overtopping device	Wave dragon	Pulsating water	overtopping seawater: gearing, ½, rectification, storage	low head hydro turbine
OWC activated oscillator	Aqua BoUY	pulsating water oscillating solid	hydraulic transmission – pulsating fluid: gearing, rectification	water turbine
Helmholtze Resonator	Resonator (Novel concept in this proposal)	pulsating water	water turbine directly driven oscillating air column: gearing	low head hydro turbine Air turbine: rectification

1.5 Motivation and Introducing a new device, named Resonator

While more than a thousand WEC's have already been designed, there is still a need to develop WEC devices that are more efficient and economical with minimal environmental impacts. Although many factors influence the efficiency of WEC devices, one of the most important factors is the geometry of the device. A more precise design in geometry can enable efficient extraction of more energy from incident waves. Present studies introduce a novel concept of a WEC device referred to as a Resonator; this device is inspired by geological "toilet bowls" and blowholes in nature—a geological phenomenon that formed as sea channels grow landwards into a water basin, which can result in a high pulsating current of water inside the channel in and out of the basin. The resonance of water inside the basin produced by asymmetry of its narrow water channel allows for the capture of Helmholtz mode of the waves, which is the most efficient mode of oscillation as it consents the device to attract the most energy. Figure 1-2 indicates an example of the toilet bowls within Hawaiian coastal region.

In principle Resonator, operates similar to OWEC [27], in which the water oscillates in a chamber. However, the geometry of Resonator is optimized to maximize the water velocity in the channel, the aimed way to extract the power using water turbine as a PTO. This mitigates noises caused by air turbine used in all OWEC devices. The design of a Resonator is simple containing no moving parts, it can be constructed with a low cost material and possesses a relatively small form factor. Thus, it maximizes wave energy while minimizing maintenance and operational costs. The concept is perspicuous: the narrow channel, basin, and specific connection between them along with a specific geometry such that allow to capture an augmented quantity of incoming wave power to be captured.

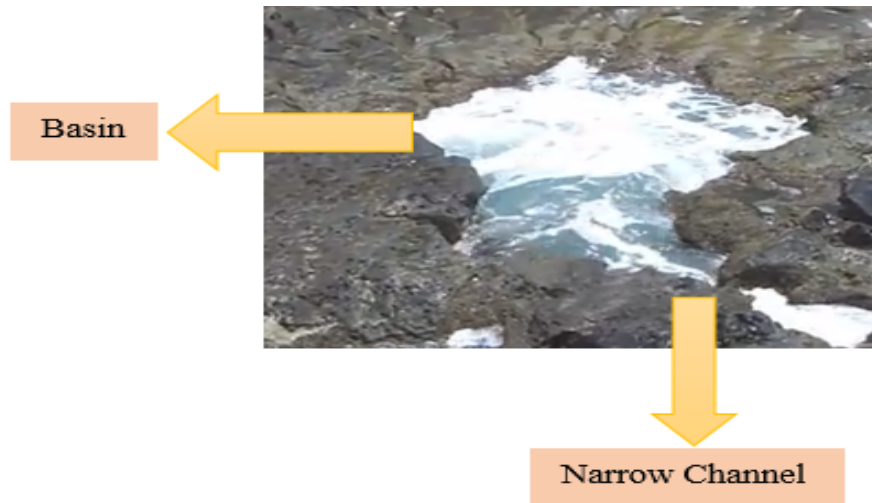


Figure 1-2: Natural Resonator at Hanauma Bay, Hawaii.

In this study two different scale models are utilized; one used a $1/25^{\text{th}}$ scale device in a flume at the University of Hawaii at Manoa while the other model used a $1/7^{\text{th}}$ scale device at the Richmond Field Station of University of California, Berkeley. The amplitude of the waves were measured using wave gauges and then collected data that showed a resonance in the channel of the device. Following this study, the $1/25^{\text{th}}$ scale device was tested with a two-dimensional Particle Image Velocimetry instrument (PIV) to determine the instantaneous velocity field through the scaled model.

CHAPTER 2: GOVERNING EQUATIONS

2.1 Governing Equations

The Helmholtz mode equations that govern this project utilize theoretical methods for tidal waves from studies by Doleman and Mass [28, 29]. This study, experimentally validated the application of tidal generated waves' Helmholtz equations toward wind generated waves' Helmholtz equations. In Fig. 2-1, the top view of a basin is illustrated with maximum depth H and horizontal area A^* , which depends on Z^*/H the non-dimensional depth of water, and is connected to the sea by a narrow strait of width B and depth H . Z^* is the vertical coordinate which is measured from the mean-water level upwards.

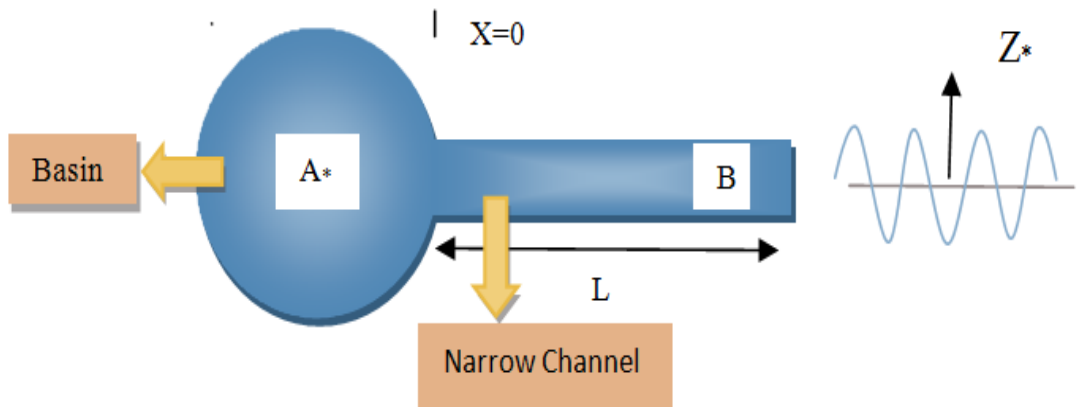


Figure 2-1: Top view of a basin with narrow channel

Maas carried out the theoretical method to examine the tidal Helmholtz resonance in the basin, assuming that the strait's length L , as well as the basin's length scale $A_0^{1/2}$, are much smaller than the tidal wavelength in the basin, λ . Thus, the tidal wave travels

through the basin momentarily, Here $A_0 = A_*(0)$. Equation (1) defines the wavelength determined by the lunar semi-diurnal tidal frequency such that:

$$\lambda = 2\pi c / \sigma_e \quad (1)$$

Where σ_e is equal to $1.4 \times 10^{-4} \text{ rad s}^{-1}$ and “c” is the long-wave speed defined by Eq. (2):

$$c = \sqrt{gH} \quad (2)$$

Where g is the gravitational acceleration and H is the basin depth.

Velocity and frictional effects are negligible for the case where the width of the basin is much greater than the width of the channel. However, this is not applied to Resonator by means of geometry and PTO in which the energy is extracted. This part can be further studied. In a relatively broad basin, since the external tide elevation at sea $\zeta_e(\sigma_e, t_*)$ is defined as a periodic function of time t_* , and the velocity and frictional effects are small, thus the momentum equations in the basin will reduce to the lowest order, stating that horizontal pressure gradients are equally negligible. Thus, the uniform Helmholtz modes are the dominant modes in the basin. In addition, the tide's state in the basin can be explained by a single time dependent parameter, like the surface elevation, ζ_i , or the volume. The excess of the volume contained in the basin is approximately given in Eq. (3):

$$V_* \equiv \int_0^{\zeta_i} A_*(Z_*/H) dZ_* \quad (3)$$

$$\frac{dV_*}{dt_*} = -u_0(H + \zeta_0)B \quad (4)$$

Where $u(x; t_*)$ is the depth-averaged flow and $\zeta_*(x; t_*)$ is the surface elevation within the strait. ζ_0 happens in the entrance of the basin ($x=0$).

The flow through the strait, as derived from the momentum equation, is shown in Eq. (5):

$$\frac{\partial u}{\partial t_*} = -\frac{\partial}{\partial x} \left(g\zeta_* + \frac{1}{2}u^2 \right) - \frac{k}{\zeta_* + H} |u| u \quad (5)$$

Where Coriolis effects are ignored and k is a bed stress coefficient.

It was assumed that the flow is uniform downstream of the channel where the width increases due to the basin, and the elevation decreases linearly over the length of the channel. It was also assumed that the change in the surface elevation is much smaller than the depth of the system. Integrating the flow equation along the length of the channel yields Eq. (6):

$$L \frac{dU}{dt_*} = g(\zeta_i - \zeta_e) + \frac{1}{2}(u_i^2 - u_e^2) - L \frac{K}{H} |u| u \quad (6)$$

Where subscript “i” refers to a variable’s value in the basin’s interior whereas the subscript “e” refers to the exterior of the basin. After several simplifications the excess volume changes in the basin can be calculated as Eq. (7):

$$\frac{dV_*}{dt_*} = -uHB \quad (7)$$

There is a dynamic pressure difference between outflow and inflow, with the inflow proportional to the channel flow $u_i = (1-\delta)u$ and the $u_e = u$,

where δ denotes an empirical proportionality constant and considering $u > 0$. Thus, for small δ we can rewrite $\frac{1}{2}(u_i^2 - u_e^2)$ as $(-\delta u^2)$ or $(-\delta |u|u)$. This pressure drop between inflow and outflow, the bottom friction in the channel, and wave radiation during the water oscillation in the basin all lead to a damping process in the Helmholtz oscillator. Due to this damping process, the length of the channel is effectively increased, as the water excess outside the strait takes part in the oscillation. Thus, the effective length becomes as Eq. (8):

$$L_E = L - \frac{B}{\pi} \left[\ln\left(\frac{\pi B}{\lambda}\right) + \Gamma - \frac{3}{2} \right] \quad (8)$$

In which $\Gamma = 0.5772$ signifies Euler's constant. Hence, the total oscillating fluid's mass increases and therefore the Helmholtz frequency decreases.

In a non-dimensionalized formula for Helmholtz frequency, we assume that $Z_* = H_z$, $\zeta_i = H\zeta$, $A_*(Z_*/H) = A_0(A(z))$, $V_* = A_0 H V$, and dimensionless excess volume is shown in Eq. (9):

$$V = \int_0^{\zeta} A(z) dz \quad (9)$$

Where, $\zeta_e = H Z_e$, and $t_* = t / \sigma H$.

Thus, the tidal Helmholtz frequency is defined as Eq. (10):

$$\sigma_H^2 = gHB / A_0 L \quad (10)$$

Considering the scales and eliminating u by combining with the linear damping term, the Helmholtz resonator due to excess volume $V(t)$ is derived such that is shown in Eq. (11):

$$\frac{d^2 V}{dt^2} + \zeta(V) = Z_e(\sigma t) - r \frac{dV}{dt} - \gamma \left| \frac{dV}{dt} \right| \frac{dV}{dt} \quad (11)$$

Here, $r = \sigma B/2L$ denotes the radiation damping coefficient, and $\gamma = (\delta/L + k/H)A_0/B$ signifies the aggregate of quadratic damping coefficients. The forcing parameters and damping parameters r and γ are independent quantities. Also, $\zeta(V)$ is the restoring term and it is a function of excess volume. The forcing by the external wave is shown in Eq. (12) and is characterized by its amplitude F and scaled frequency $\sigma = \sigma_e/\sigma_H$.

$$Z_e = F \cos \sigma t \quad (12)$$

CHAPTER 3: Experimental set up

As introduced earlier, the theoretical model above is examined through two different experiments, using wave gauges in wave tanks for 1/25th and 1/7th scales, measuring the amplitude of the waves, and using PIV instrument to determine the instantaneous velocity field. Subsequent, all the experiments are fully described and the results are clearly discussed.

The experiments validate the application of tidal generated wave Helmholtz equations for wind generated wave resonance under the following assumptions:

- The square-root of the basin's area is much smaller than the wavelength of incoming waves.
- The Froude number can be applied to the Helmholtz resonance mode. This allows a geometric factor, λg , of 25 and 7 to be applied to the Helmholtz frequency, σ_H , scaling it by $\frac{1}{\sqrt{\lambda g}}$.
- The surface elevation for a progressive periodic wave is sinusoidal and is a function of position x and time t that is indicated in Eq. (13):

$$\eta(x, t) = a \cos(kx - \omega t) \quad (13)$$

Where a is the wave amplitude and $k=2\pi/L$ denotes the wave number. The angular frequency is $\omega = 2\pi/T$, where T is the wave period.

- The time averaged power of the incoming wave into the device of width W_f is shown in Eq. (14):

$$P_1 = \frac{1}{2} W_f \rho g \zeta_e^2 C_g \quad (14)$$

Where, C_g is the group velocity and $C_g = (gH)^{0.5}$.

- The power at the channel is defined as Eq. (15):

$$P_c = \frac{1}{2} \rho B H U^3 \quad (15)$$

- The power in the basin is calculated by Eq. (16):

$$P_2 = \frac{1}{2} W_f \rho g \zeta_i^2 \sigma_H. \quad (16)$$

- Thus, the ratio of power in the basin to the power of the incoming wave is defined as Eq. (17):

$$\frac{P_2}{P_1} = \left(\frac{\zeta_i}{\zeta_e} \right)^2 \sqrt{\frac{W_b B}{W_f H L}} \quad (17)$$

where W_b is the length of a square shaped basin, assuming the square profile.

3.1 1/25th scale set-up

In the case of the 1/25th scale experiment, the wave flume was 0.15 m wide and sufficiently long for the experiment. The channel width was 0.05 m and the water depth was 0.2 m. The sketch of the proposed design is shown in Fig. 3-1.

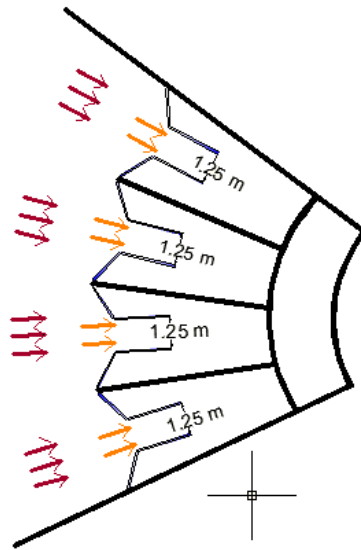


Figure 3-1: A sketch of the proposed design.

and the views from the top and side of the experimental design are shown in Fig. 3-2, however this design was modified after the preliminary results.

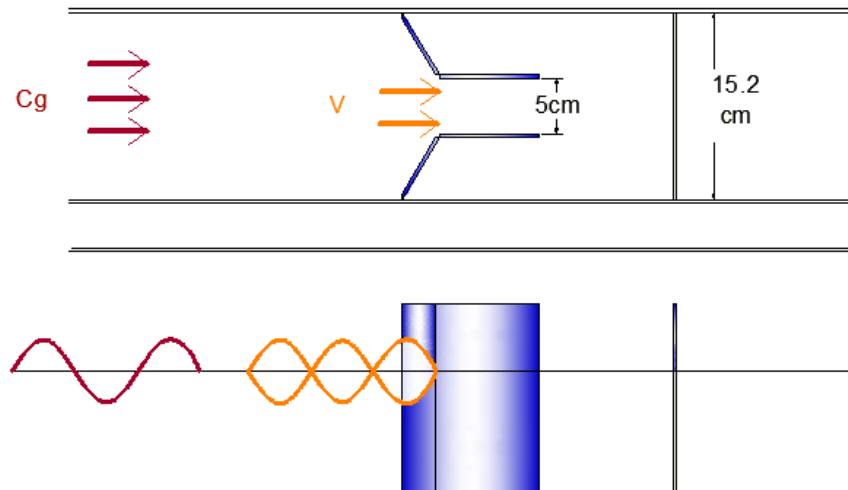


Figure 3-2: A sketch of the top and side views of the experiment.

Wave height was measured using three JFE Advantech high sensitivity capacitive wave level sensors (ACH-600RS) with a resolution of 0.1 mm and an accuracy of ± 0.03 mm. Data collection was at a nominal 72 Hz. The first wave gauge was positioned at a distance greater than three water depths from the wave maker, measuring fully developed incident wave height basin. It was also spaced exactly one wavelength from the third wave gauge so as to determine the phase-shift between basin free surface and incident waves. The second wave gauge was suspended in the channel of the resonator, and a third in the middle of the basin. Wave gauges locations are shown below in Fig. 3-3.

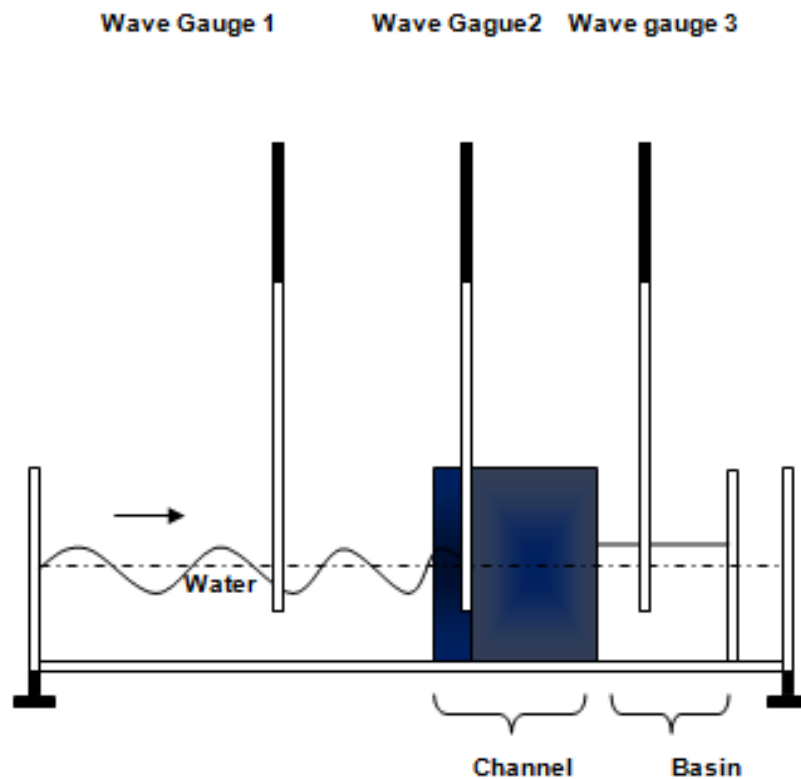


Figure 3-3: Location of the three wave gauges

Periodic linear intermediate waves were produced using a computer-controlled wave maker in the flume. Target ocean wave periods of 4.5 to 7.5 seconds were scaled to 0.9 to 1.5 seconds using a geometric factor of 25, and wave height was 20% of the water depth. The resonator basin channel was oriented parallel to the direction of travel of the incident waves. The width of the channel was reduced relative to the flume width using angled winglets, whose lengths and thus angles were varied. Using this set-up, two sets of experiments were conducted, and in each case the area of the basin was adjusted to match the Helmholtz resonance to the incoming wave frequency. The first set of trials tested the full period range (0.9 to 1.5 seconds) with a single winglet configuration. The purpose of this was purely to determine the period's effect on the Helmholtz resonance, and resulted in correlation between the wave period and Helmholtz resonance. The second set of trials tested a range of winglet angles with a static period of 1.4 seconds. The winglet angles ranged from 60 to 25 degrees, as measured from the flume wall. The channel consisted of a straight section of reduced width relative to the wave flume and oriented parallel to the direction of travel of incident waves. Channel reduces its width through the employment of winglets. For the experiment, the lengths of the winglets were varied to determine the effects of the angle of reduction on the incident, reflected, and transmitted waves.

Three experiments were conducted. The first utilized the full period range (0.9-1.5 seconds) and one winglet size (Winglet 1) to determine the periods affect on the Helmholtz resonance.

The area of the basin was adjusted to match the Helmholtz resonance of the basin to the incoming wave frequency. The first utilized the full period range (0.9-1.5 seconds) and one winglet size to determine the periods affect on the Helmholtz resonance.

The second experiment utilized the full winglet range and a static period of 1.4 seconds. The winglet angles were measured relative to the flume wall and ranged from 60° to 30°. Table 3-1 displays the specifications for the winglets used.

Table 3-1: Winglet Sizes used in the experiment and the corresponding angles.

Winglet	Length [mm]	Angle Relative to Flume Wall
1	70	60
2	99	42
3	125	30

This experiment explored the effect of the angle of channel reduction to the performance of the system, a factor not considered in the model. This experiment explored the winglets' affect on phase shift between incident waves and the basin oscillations, the ratio of incident wave height to magnitude of basin oscillation, and the reduction angle's effect on the reflected and transmitted waves in the system.

Table 3-2 reflects the conclusions drawn for the second experiment. With Winglet 1 the channel reduction angle was the greatest and caused flow to change abruptly. This drastic channel reduction angle led to larger-amplitude reflected waves at the face of the channel and thus a reduction in wave energy transmitted to the basin, and higher harmonics in the overall systems. The case with Winglet 3 showed that the lower reduction angle reduced these higher harmonics and allowed for more energy to be transmitted to the basin.

Table 3-2: Table of the Ratios of Gauge 3 to Gauge 1 and the respective winglet

Winglet	Ratio of Gauge 3:Gauge 1
1	1.069
2	1.082
3	1.322

It was found that a lower reduction angle corresponded to a reduction of higher harmonics, allowing more energy to be transmitted to the basin.

The experiments above resulted in fabricating and testing the final device for 1/25th scale. This device has the lower reduction angle that means $\theta = 30^\circ$ and also, the winglets are curved causing much more efficient device with lower energy dissipation. The final device diagram is shown in Fig. 3-4.

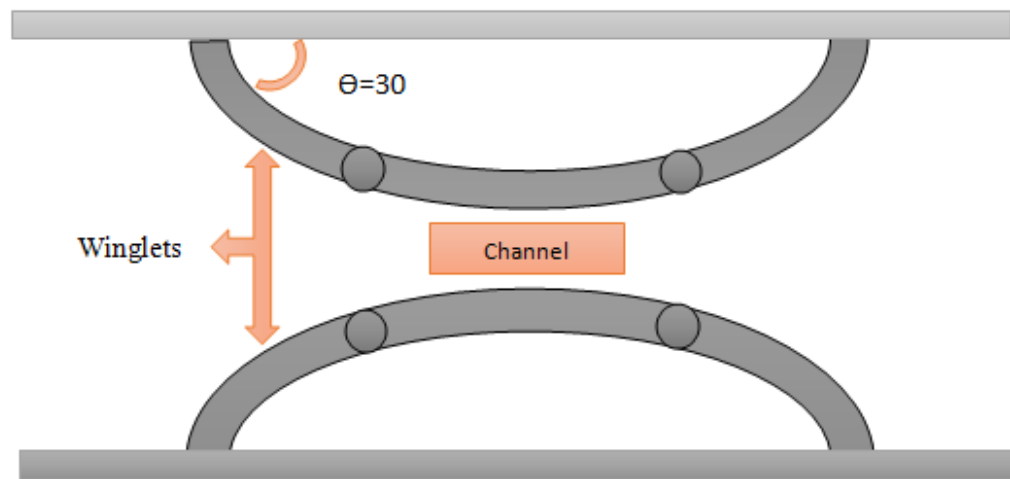


Figure 3-4: Top view of the length and angle of winglets

Another set of experiments explored the performance of the systems when a one-way gate was added to the channel at the entrance to allow the incident wave to enter the basin but requiring the exit flow out below the water surface. Adding the one-way gate significantly improved the ratio between basin wave amplitude and incoming wave amplitude showing a reduction of friction damping in the channel. It was observed that the exit flow was augmented due to the gate, which could lead to performance gains when a turbine is implemented.

Final experiments characterized the dynamic performance of the system when the channel was partially blocked, representing the resistance flow due to hydrodynamic dampening of a submerged turbine. The one-way gate was employed to induce exit flow past the location of a turbine. Three different blockage ratios of 40%, 60%, and 80% of the channel cross-sectional area were used. These blockages did not significantly affect

the dynamics of the system since no significant phase shifting occurred. However, it was seen that, of the case explored, the 80% blockage caused the greatest magnitude of reflected waves of the case explored. This directly affected the energy transmitted and the flow velocity in the channel. Conversely, the 40% blockage affected flow velocities least and resulted in the lowest magnitudes of reflected waves.

3.2 Analysis and results of 1/25th scale device

The data was processed using Matlab to determine the phasing of incident waves relative to the wave level in the basin. Theoretically, the two locations will be in phase at both locations signifying resonance in Fig. 3-5 the system as in that illustrates a sample of data for the three wave gauges.

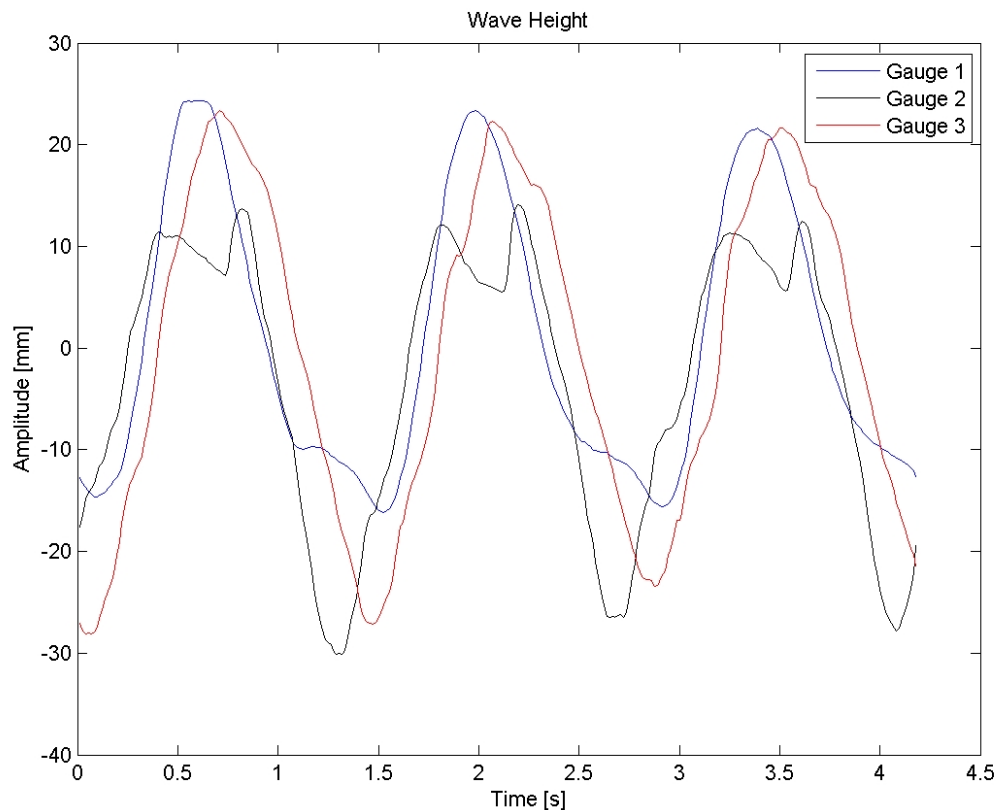


Figure 3-5: Wave Gauge Sample Data

Using the recorded wave heights the data was transformed to the frequency domain. The magnitudes of the signals' frequencies were not significant. Fig. 3-6 shows a sample of how the dominant frequencies for the gauges were determined.

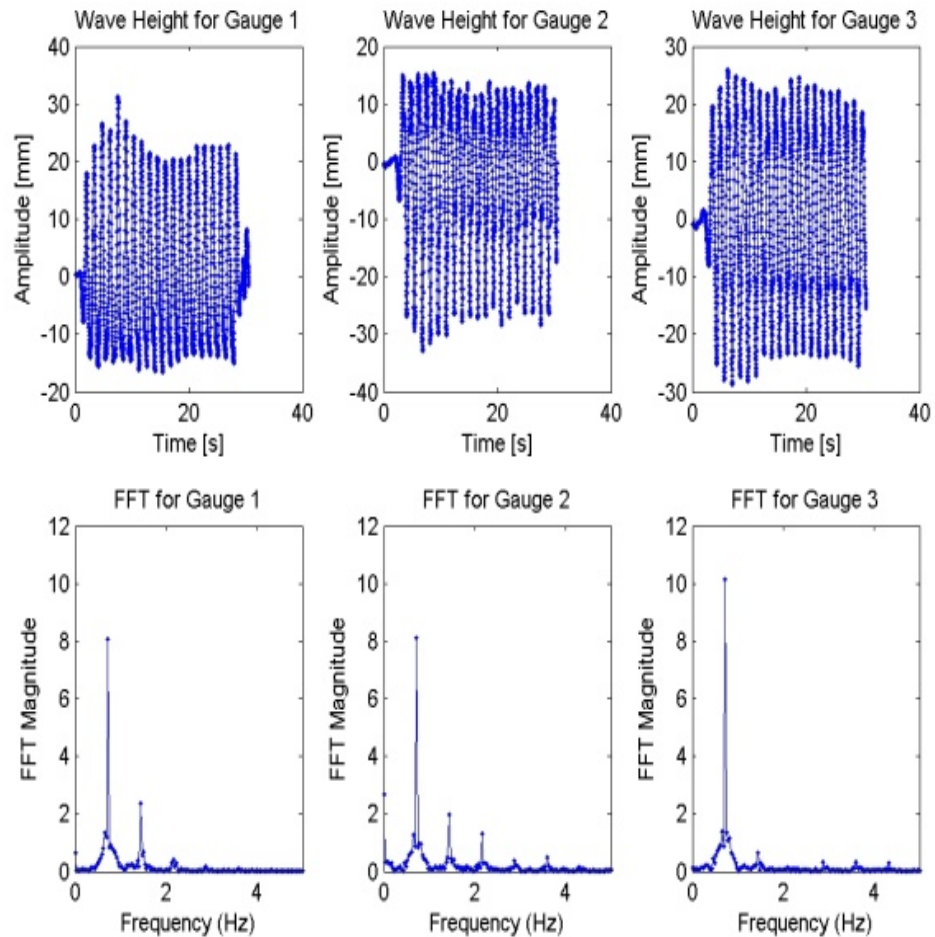


Figure 3-6: Sample of dominant frequency

This experiment was purely to determine the validity of the theoretical model. The correlation of theoretical and experimental periods of the Resonator is shown in the Fig. 3-9, which demonstrates that the theoretical tidal model closely describes the wave model. The 29% increase in natural frequency of the basin is caused by an increase in channel length affected by the winglets.

After the signal has been transformed into the frequency domain and represented as a complex array and before the signal has been normalized into a real array the phase angle of the signal was determined for each respective frequency. Figure 3-7 illustrates the curve resulting from this method.

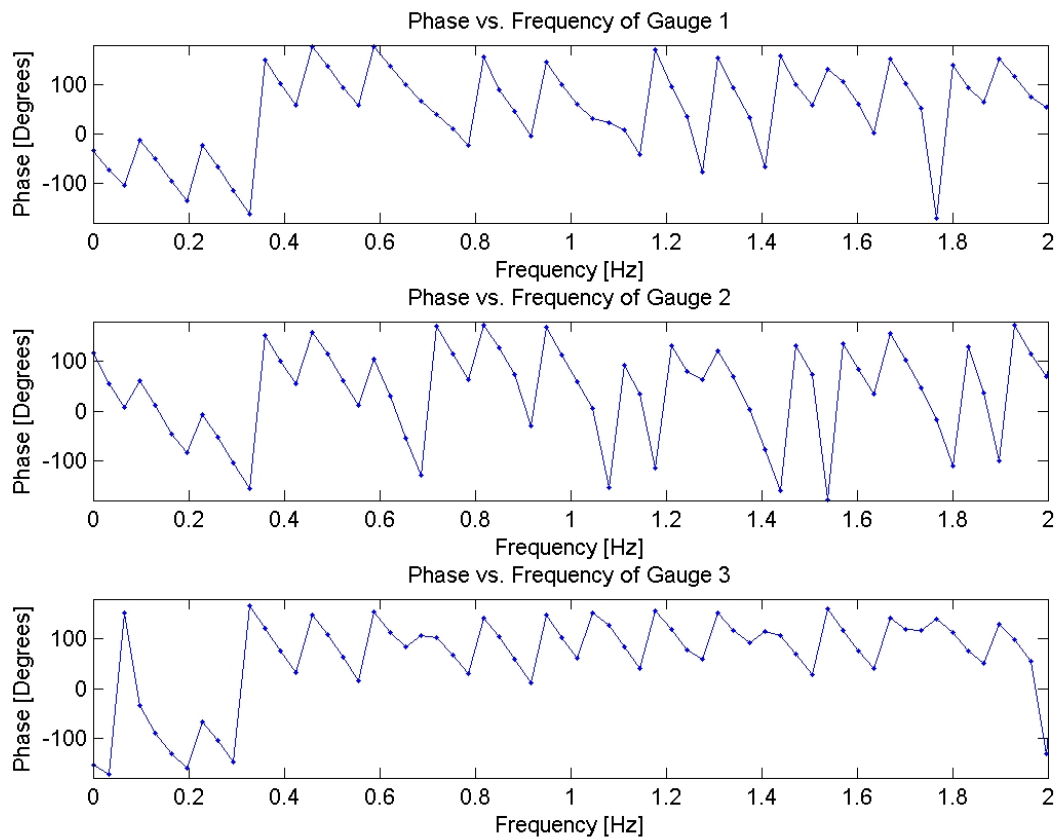


Figure 3-7: Phase Angle of the Signal for Each Inherent Frequency.

Figure 3-8 shows the phase shift of the three pairs of signals. Of interest is the Gauge 1 Gauge 2 phase shift. The dominant frequency and its corresponding phase shift are determined.

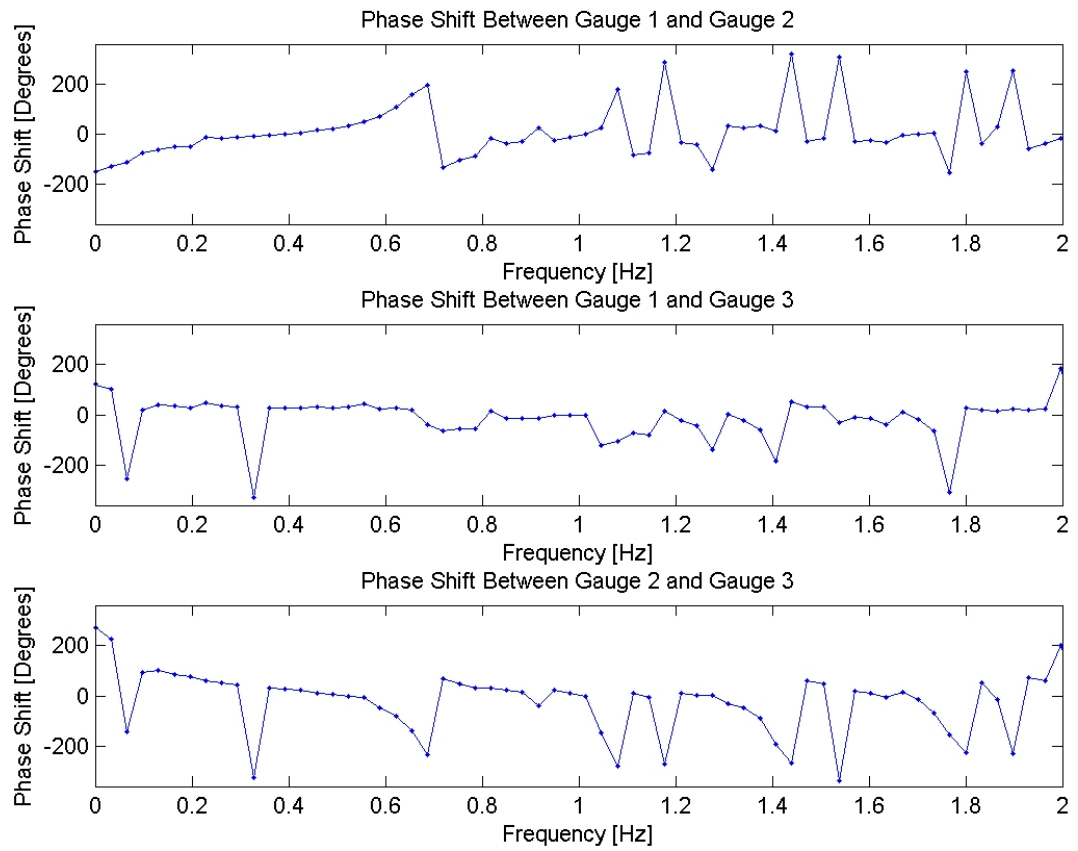


Figure 3-8: Phase Shift of the three combinations of signals.

A comparison of the phase shift values for a range of horizontal basin areas for each period was conducted for each period and winglet combination. As mentioned in the previous section, the horizontal basin area is directly related to the distance of the basin plate to the channel that was varied to determine the accuracy of the theoretical model. The following section shows the accuracy of the model to experimental data.

This experiment was purely to determine the validity of the theoretical model. The correlation of theoretical and experimental periods of the Resonator is shown in the Fig. 3-9, which demonstrates that the theoretical tidal model closely describes the wave

model. The 29% increase in natural frequency of the basin is caused by an increase in channel length affected by the winglets.

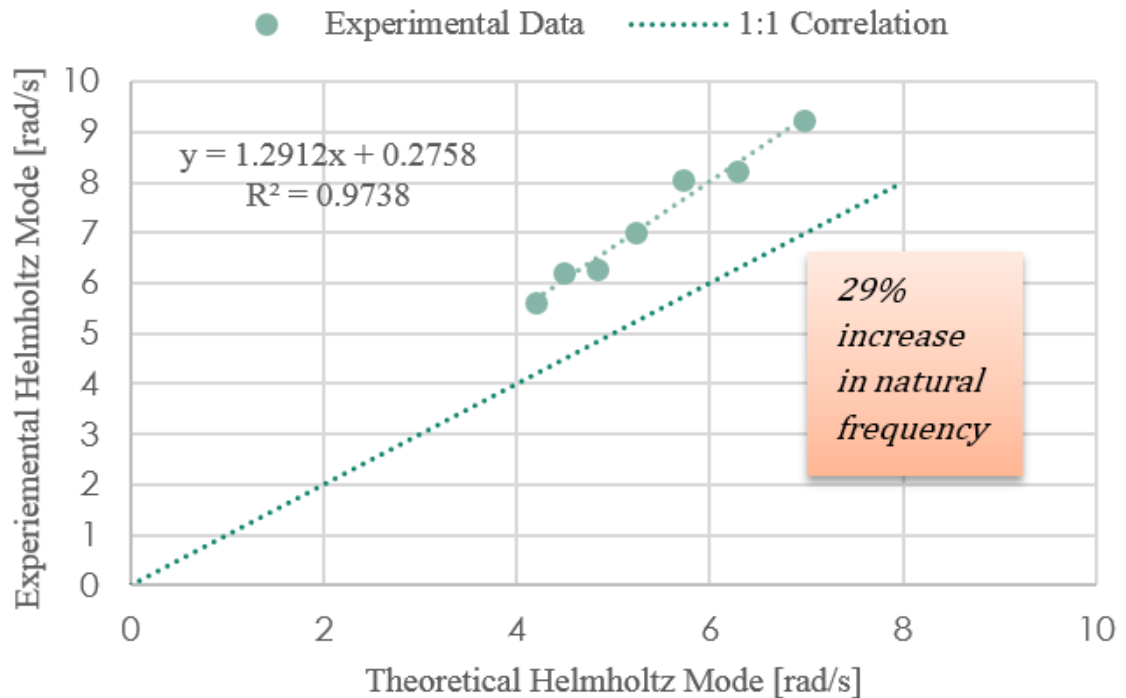


Figure 3-9: Theoretical and Experimental Comparison of Helmholtz Mode.

The second experiment showed the effect of different winglets on the performance of the system. With Winglet 1 the channel reduction angle was the greatest and caused flow to abruptly change. This drastic channel reduction angle leads to larger amplitude reflected waves at the face of the channel resulting in a reduction in wave energy transmitted to the basin and higher harmonics in the overall systems. The case with Winglet 3 showed that the more shallow reduction angle reduced these higher harmonics and allowed for more energy to be transmitted to the basin. These are shown in Fig. 3-10.

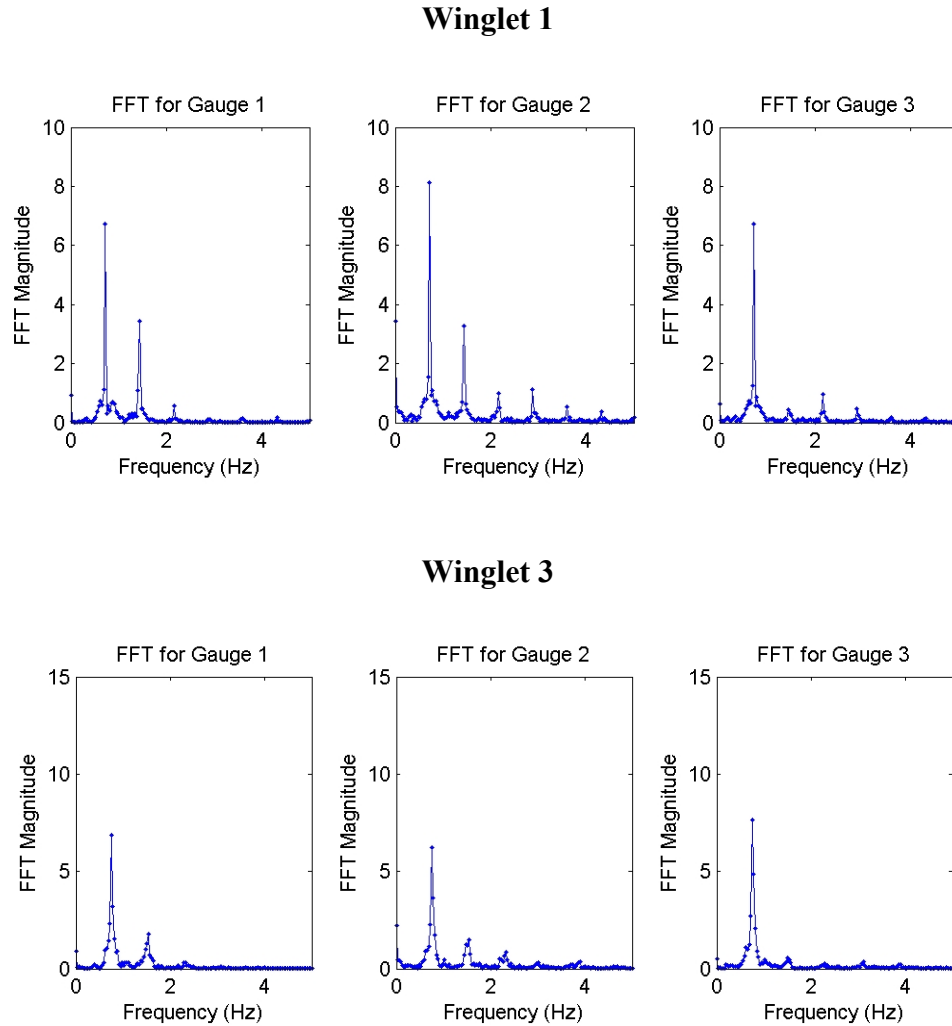
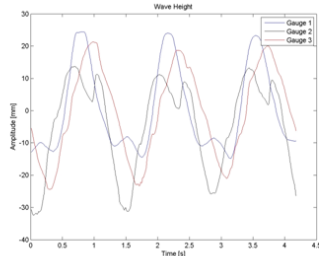


Figure 3-10: Results of the Second Experiment exploring the effects of channel reduction angles through the implementation of a range of winglets.

The third experiment showed promising results for future large scale testing with the use of a submerged turbine. The one-way gate was employed to induce exit flow past the location of a turbine. Figures (3-11 to 3-14) show the use of such a gate did not have any significant negative effect on the performance of the system. It was observed that the exit

flow was augmented due to the gate, which could lead to performance gains when a turbine is implemented.

Channel With Flap



Fourier Transform of Channel with Flap

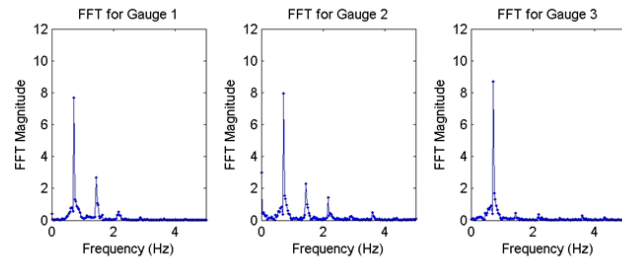
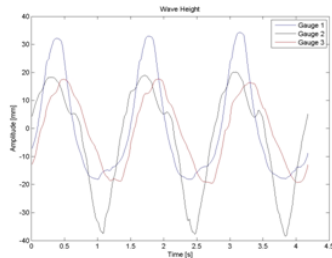


Figure 3-11: Third Experiment exploring the arbitrary implementation of a one-way gate and channel blockage to represent the resistance of flow posed by the use of a submerged turbine. (Flap)

Channel With Flap and 40% Blockage



Fourier Transform of Channel with Flap and 40% Blockage

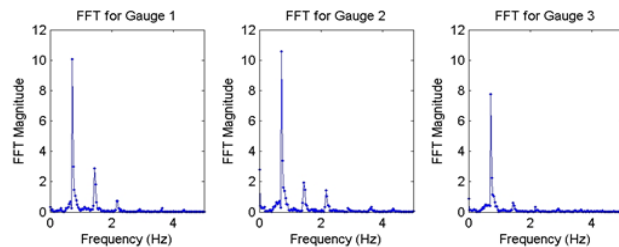
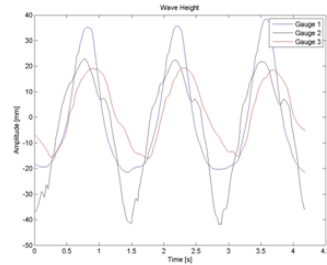


Figure 3-12: Third Experiment exploring the arbitrary implementation of a one-way gate and channel blockage to represent the resistance of flow posed by the use of a submerged turbine. (40%)

Channel With Flap and 60% Blockage



Fourier Transform of Channel with Flap and 60% Blockage

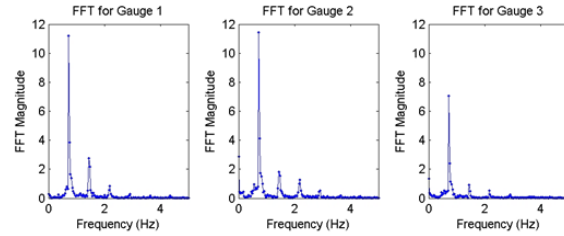
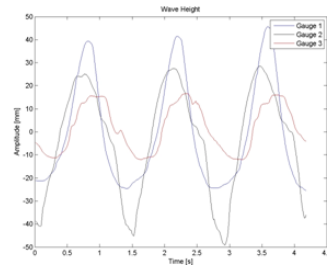


Figure 3-13: Third Experiment exploring the arbitrary implementation of a one-way gate and channel blockage to represent the resistance of flow posed by the use of a submerged turbine. (60%)

Channel With Flap and 80% Blockage



Fourier Transform of Channel with Flap and 80% Blockage

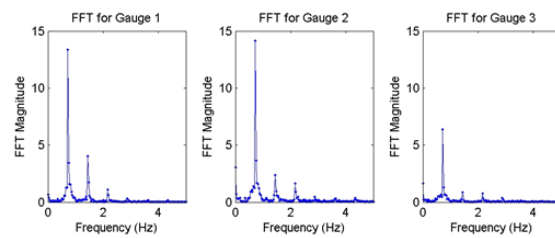


Figure 3-14: Third Experiment exploring the arbitrary implementation of a one-way gate and channel blockage to represent the resistance of flow posed by the use of a submerged turbine. (80%)

The blockage of the channel simulated the flow dampening the system may encounter when a turbine is installed. The blockages were 40%, 60%, and 80% of the channel

cross-sectional area. These blockages did not significantly affect the dynamics of the system since no significant phase shifting occurred. However, it was seen that the 80% blockage caused the greatest magnitude of reflect waves of the case explored. This directly affected the energy transmitted and the flow velocity in the channel. On the contrary, the 40% blockage affected flow velocities the least and resulted in the lowest magnitudes of reflected waves.

3.3 1/7th scale set-up

Two wave gages were used in this setup. The first was positioned at a distance greater than three water depths from the winglets, to measure fully developed waves, and one wavelength from the second wave gage, in order to determine phase shift between incidence waves and the basin free surface. The second wave gauge was suspended in the middle of the basin.

The wave periods tested were scaled using a geometric factor of 7, such that the target oceanic periods of 4.5 to 7.5 seconds were scaled to 1.7 to 2.84 seconds. The basin was built to resonate at 2.4 seconds, therefore testing was done primarily at this frequency. The device was constructed using plywood panels on a frame of aluminum extrusions, with dimensions of 1 meter wide by 1 meter tall by 1.3 meters long and with the channel width of 0.3 meters and the winglet angles $\theta=30^\circ$ that resulted as the most efficient angle from previous experiment for 1/25th scale. The device is shown in Fig. 3-15. The flume was 2.46 meters wide and 1.99 meters tall and adequately long for the experiment. More details can be found in [30].

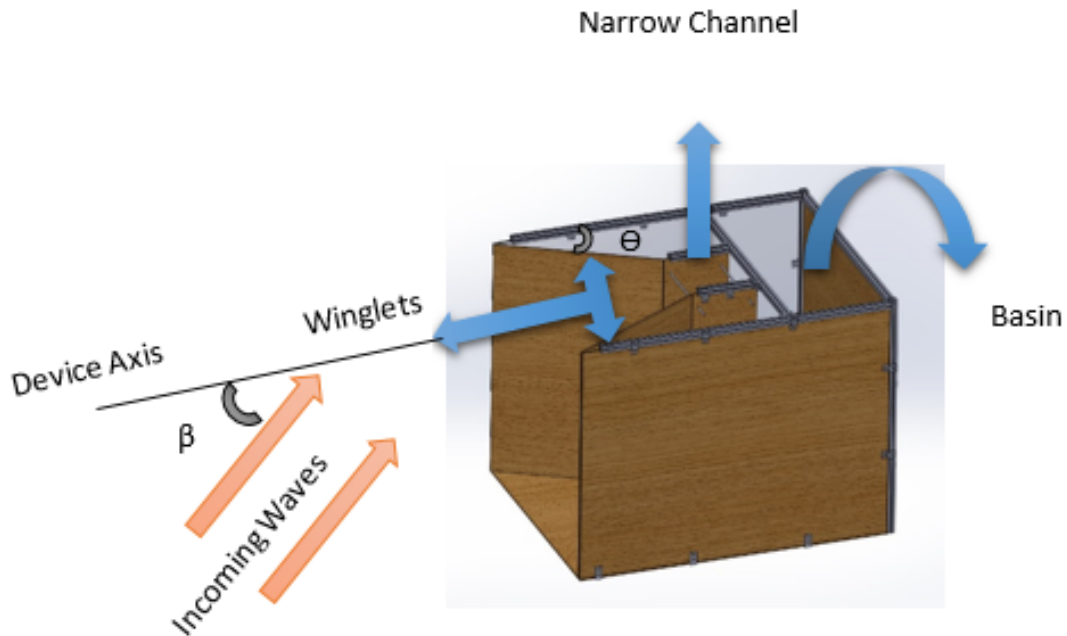


Figure 3-15: The experimental device at 1/7th scale.

Two capacitive wave gauges were used to record the wave heights. The first wave gauge was positioned at distances greater than three water depths from the wave maker to measure the fully developed incident waves, and maintained a distance of one wavelength from the second wave gauge inside the middle of basin to determine the phase shift between incident waves and the basin free surface.

The periods tested were scaled using a geometric factor of 7 such that the target ocean period range of 4.5-7.5 seconds was scaled to 1.7-2.84 seconds in the experiments. Testing was primarily done with a 2.5 second period, as the basin was built to resonate at this frequency.

In addition to validating the theoretical model as was done in the first experiment, the basin was rotated by 15 degree increments from 0 degrees to 45 degrees relative to the flume wall in order to ascertain the effect of angle of incidence on internal wave height. As expected, 0 degrees produced the greatest basin wave height. Fig. 3-16 shows the amplitude of the incoming wave and the basin at the resonance frequency.

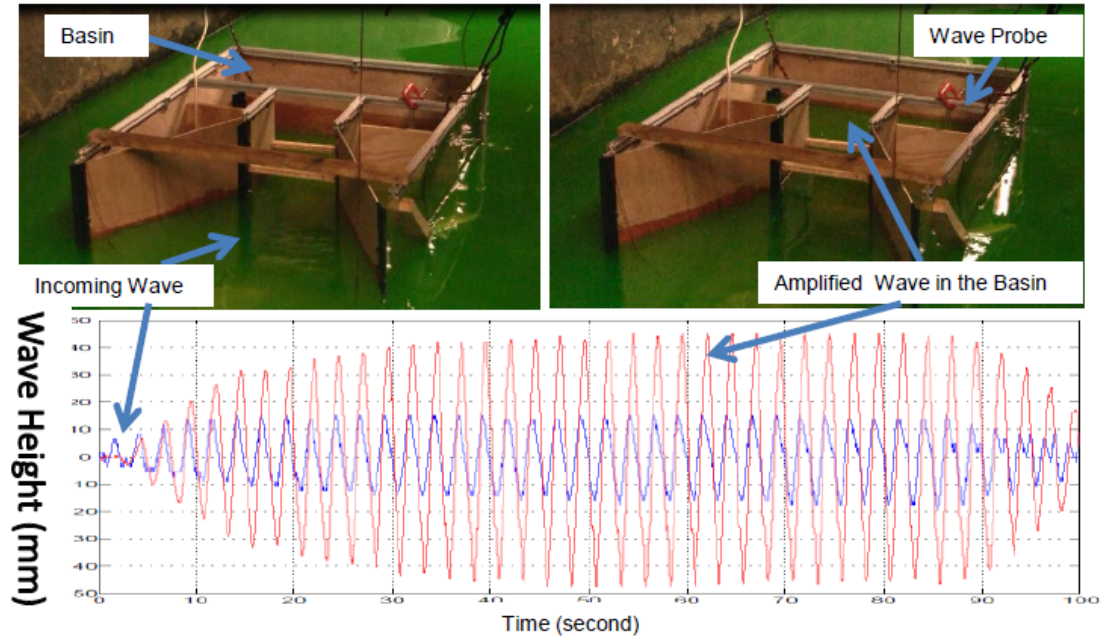


Figure 3-16: 1/7th scale model of the Resonator with response plot.

3.4 Analysis and results of 1/7th scale device

For this scale, the ratio of power in the basin to incoming wave power reduces to the equation below (Eq.17):

$$\frac{P_2}{P_1} = .5 \left(\frac{\zeta_i}{\zeta_e} \right)^2 = 4.5 \quad (17)$$

It was found that power addition to the resonator basin decreased exponentially from 100% at wave 0 to 0% (steady state) at wave 20. This is assumed to be due primarily to radiation and friction damping of the resonator.

The power ratio versus wave number data for each of the three angles of incidence is shown in Fig. 3-17. Again, it can be seen the energy absorption of the resonator saturates at around 20 wave cycles it means we cannot increase power more and it will be constant after that. It is thus between the interval of 1 and 20 wave cycles that a power take-off (PTO) should be engaged, so as to avoid energy extraction in a saturated system. Note that a PTO will affect the response and oscillation amplitude of the system—something to be investigated in further studies. More details can be found in [31].

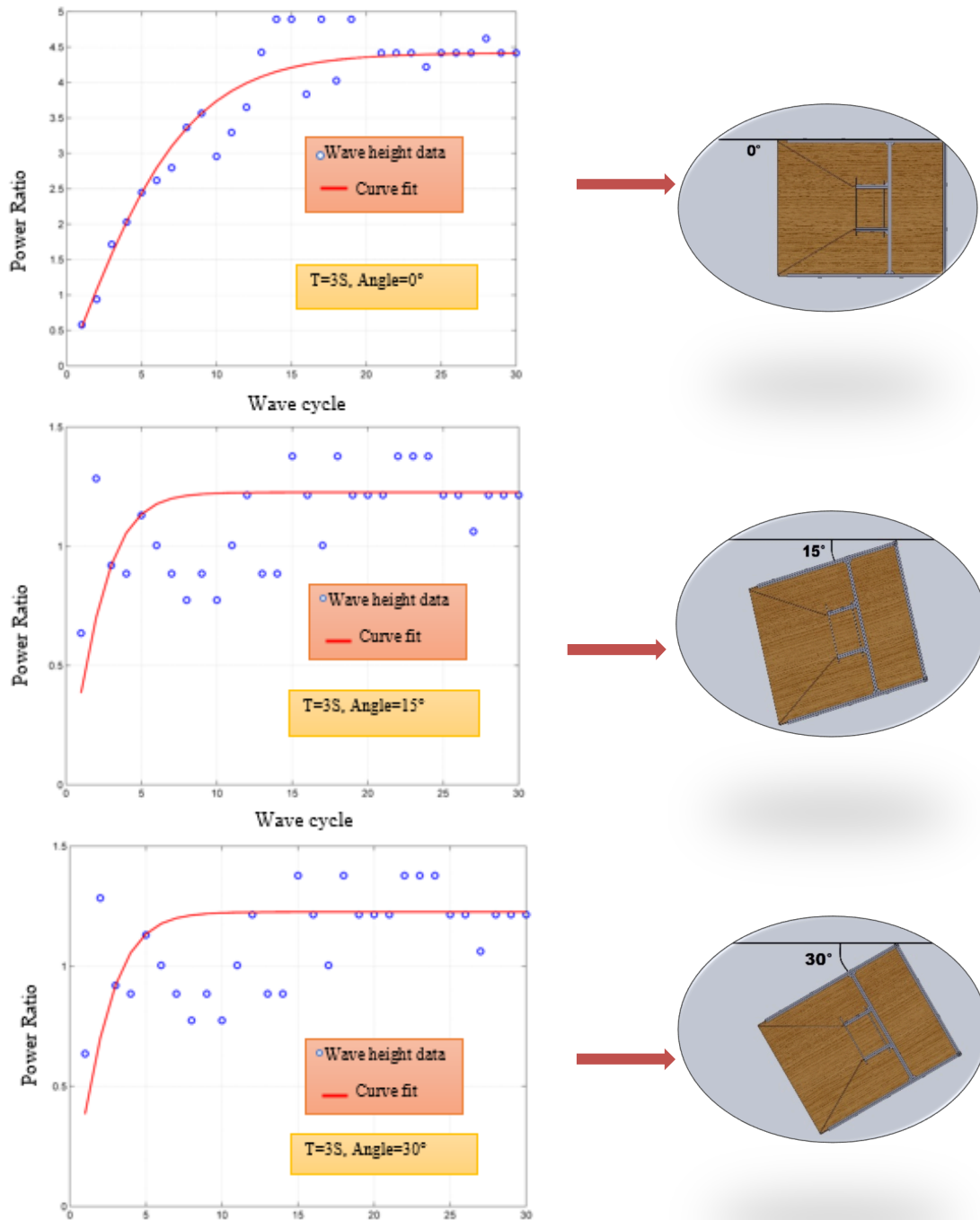


Figure 3-17: Power ratios of basin wave heights to incoming wave heights for three angles of incidence, from top to bottom: 0°, 15°, and 30°.

As shown in Fig. 3-17, the ideal power ratio occurs at 0-degrees. For this case, as explained above the system is found to become saturated at 20 wave cycles, after which the power within the system will no longer increase. Thus the optimal energy extraction interval is between the first and twentieth incident waves. It is during this time that the power take-off (PTO) be engaged so as to avoid energy extraction in a saturated system.

There are two major methods of extracting the energy from the Resonator, as shown in Fig. 3-18:

1. By using a water turbine at the channel. This method is ideal when the dominant wave period is low and wave amplitude is high, leading to high velocity within the channel. PIV has been used to measure the pulsating velocity at the channel for the 1/25th scaled model. The peak velocity was 0.6 m/sec for a wave period of 0.9 seconds and amplitude of 0.02 m. This is equivalent to a 3 m/s peak channel velocity at full-scale, with an ocean wave amplitude of 0.5 m. However, the nonlinear effect of incoming wave amplitude on the channel velocity must be investigated. This type of power take off is shown as “PTO1” in the Fig. 3-18.
2. By using an air turbine at the basin, which is shown as “PTO2” in the Fig.3-18.

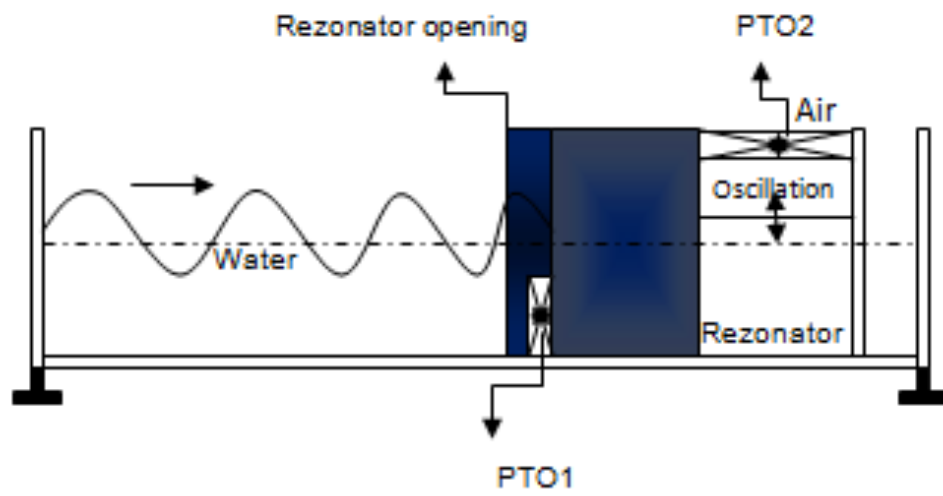


Figure 3-188: Power –Take off in the Resonator

CHAPTER 4: PIV Experiment

A flow measurement technique known as 2D Particle Image Velocimetry (PIV) was used to determine the instantaneous velocity field through the scaled model. Use of optical measurement methods for flow measurement for scaled models have several advantages.

One advantage of optical measurements is the ability to measure flow without interference. Unlike mechanical measurement probes that occupy a space within the flow, optical methods view the flow through the implementation of tracers. Another advantage, in the case of optical measurements via PIV, is a flow field is established. This is useful for flow visualization as well as flow field qualification, unlike the flow visualization methods whose characteristics are solely qualitative.

For this experiment, first it was essential to use optical methods of measurement because the small size of the model restricts the use of mechanical-type probes. Second, a flow field throughout the model was sought to determine the characteristics of flow based on depth. In this experimental work 1/25th scale model is used.

4.1 Experimental Equipment

The experiment was conducted using a commercially available PIV system from TSI, Incorporated. The components of the system were the laser, camera, synchronizer, and software.

The laser subsystem was a pulsed Dual Nd: YAG laser operating at 532 nm. The laser emits 100 mJ/pulse for a duration of 6 ns. The flashlamps of laser operate at a maximum frequency of 15 Hz. The dual laser system allows the system to then sample at 30 Hz as the two lasers operate in an alternating pulse pattern.

A The Power view HS-560 camera was used. The CCD array allows for 1280 x 1024 pixel images (1.3 mega pixels). The pixel size is 12 μm (H) x 12 μm (V), allowing for an image size of 15.4 mm (H) x 12.3 mm (V). The frame straddling interframe time of this camera model has a minimum of 75 ns, sufficient for these experiments.

The lens used was a Sigma 105mm F2.8 macro lens. The magnification of the lens is 1:1 and provides the appropriate particle clarity and depth of field for the desired results.

The synchronizer was TSI's LaserPulse Synchronizer model number 610035 which allows the computer to interface with the dual laser system, camera, and computer.

The software used was Insight 3G for data acquisition and analysis. Tecplot and Matlab were also used for processing the data provided from Insight 3G.

Additional equipment used was a light arm, cylindrical lens, and spherical lens. The light arm allowed the laser sheet to be oriented in any manner required by routing the laser through a fiber channel. The cylindrical lens used had a -50 mm focal point. The spherical lens used had a focal length of 200 mm.

4.2 *Experimental Equipment*

A diagram of the experimental setup is shown in Fig. 4-1. The optical method of 2D PIV utilizes a thin laser sheet to illuminate the 2D plane under investigation. However, water is transparent so tracer particles were required to diffract the laser to the camera. The tracer particles used were neutrally-buoyant silver-coated glass spheres. Seeding particles mixed in the fluid are illuminated when passing through the laser sheet.

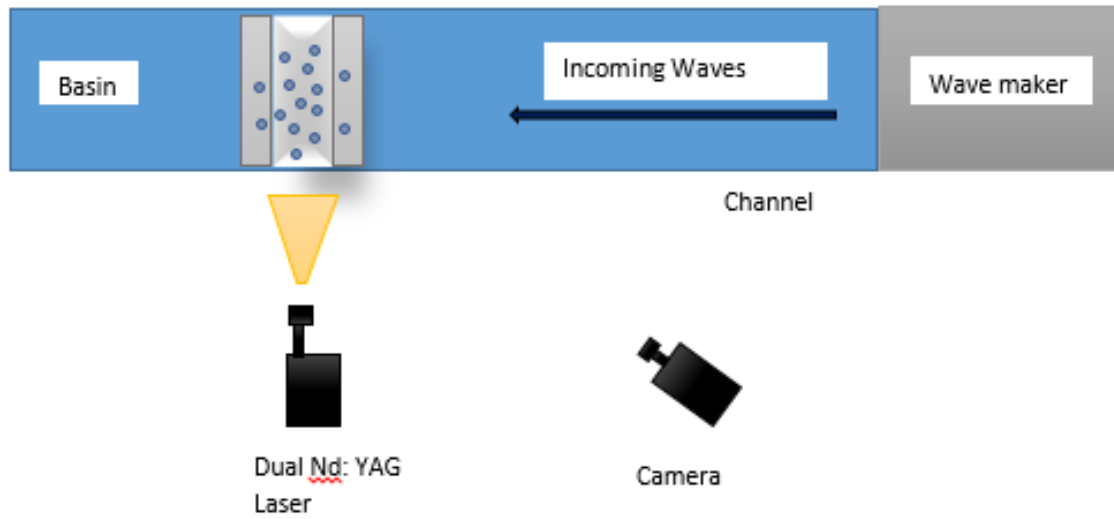


Figure 4-1: PIV Experimental Setup

The points of light are captured by a 1.3 megapixel CCD camera with a line of sight orthogonal to the light sheet. The camera exposure straddled the laser pulse in order to determine the direction of the particles resulting in two images per frame. The scaled model was fabricated from plexiglass. The model was transparent and allowed the camera to view directly into the channel capturing the flow field.

4.3 Experimental Conditions

The model was 50 mm in width at the channel. The light sheet was positioned in the middle of the channel such that light sheet was parallel to the channel walls. The light sheet was produced from an 8 mm laser beam emanating from the laser housing.

The laser beam was modified using a cylindrical lens and spherical lens, respectively. The cylindrical lens diverged the laser beam in one direction (height) while maintaining the beam dimension in the other direction (width). A light sheet of approximately 40 mm was created using a -50 mm cylindrical lens. The spherical lens determines the focal distance of the waist, the minimum laser thickness ($<1\text{mm}$). The spherical lens used had a focal length of 200 mm.

The seeding of the fluid was accomplished using silver-coated glass spheres. The mean thickness of these spheres was 10 microns and a specific gravity of 1.03, very similar to the fresh water used for the experiment. Because the two materials were close in specific gravity the translations of particles due to buoyancy was small relative to the translation due to the waves.

The camera's lens aperture ($f/\#$) that f is focal length and $\#$ is f-stop was set to 100/16. This yielded a diffraction limited spot size of 20.8, based on $Diff Spot = 2.44 * \lambda * f/\#$ where λ is the laser wavelength, $f/\#$ as discussed is the lens aperture, and Diff Spot is the resulting diffraction limited spot size. The depth of field is expressed as $DOF = 2 * D^2 * \frac{\beta}{A}$ where D is the object distance, A is the lens aperture, and β is the angular blur defined as $\beta = \frac{B}{ImgD}$ where $ImgD$ is the image distance and B is the acceptable blur size on the CCD chip. The image calibration was determined to be 198.8 $\mu\text{m}/\text{pixel}$

The wave periods under investigation ranged from 0.9-1.5 seconds. This period range was determined through the use of the geometric scaling factor of 25. The water depth was a constant 200 mm for all tests and the wave height was a constant 20 mm for all periods.

Figure 4-2 shows a snapshot of the 1/25th scale results during the PIV experiment. This image corresponds to period of 1.5 seconds for a basin length of 220 mm.

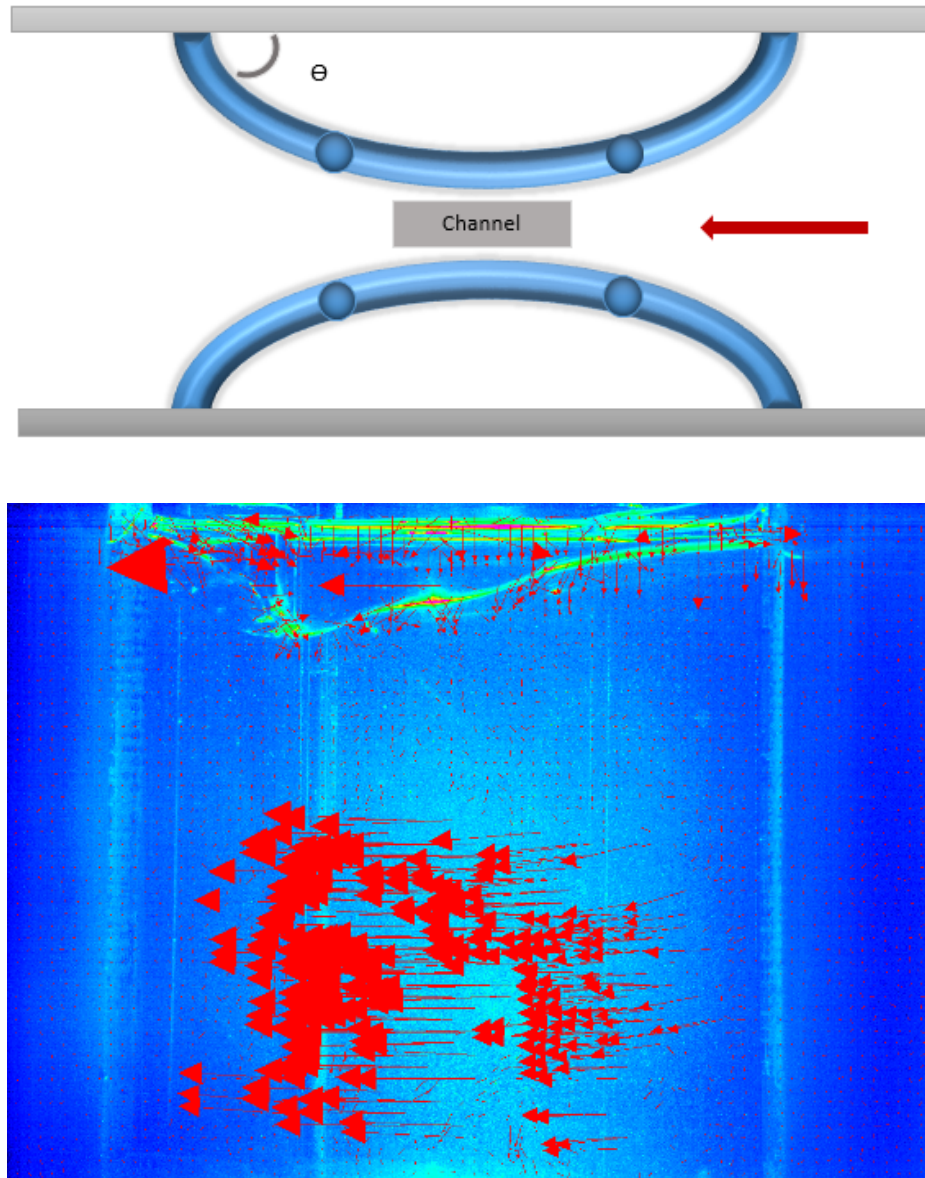


Figure 4-2: Top view and side view of device, the bottom figure is PIV image for $T = 1.5$ Sec.

The PIV camera is able to record the velocity vectors, and provide sufficient information to meaningfully interpret the results. The images of group velocity vectors at constant wave length with a period of 1.5 second are shown in Fig. (4-3, 4-12) for a short range of times.

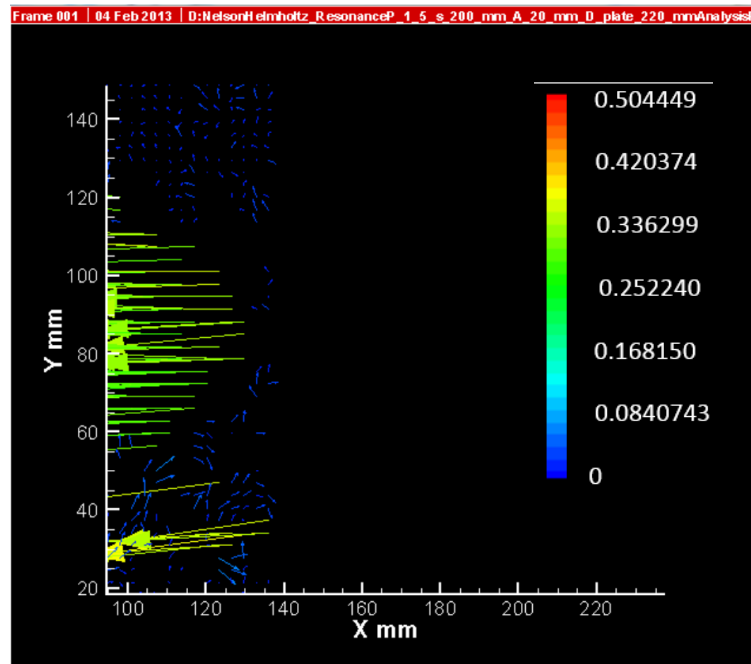


Figure 4-3: Velocity vectors after 1/6 sec.

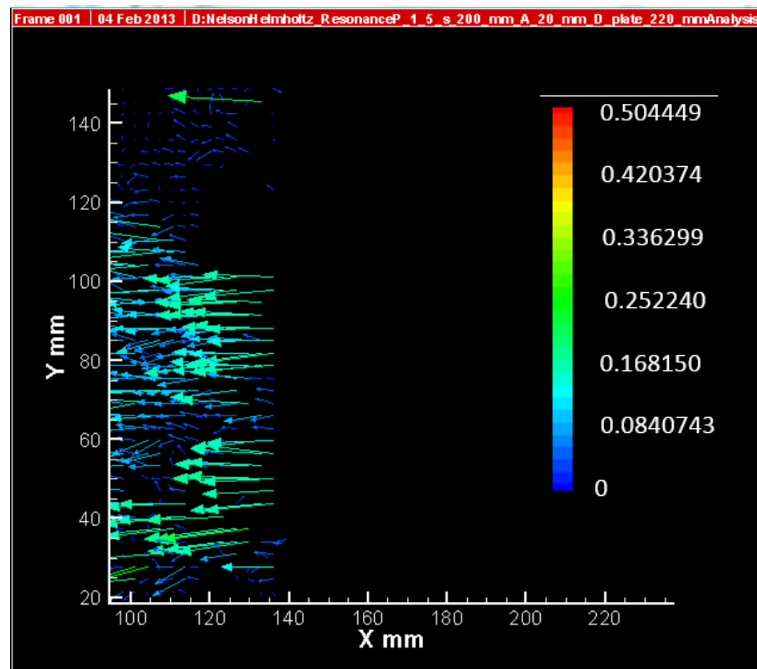


Figure 4-4: Velocity vectors after 1/3 sec.

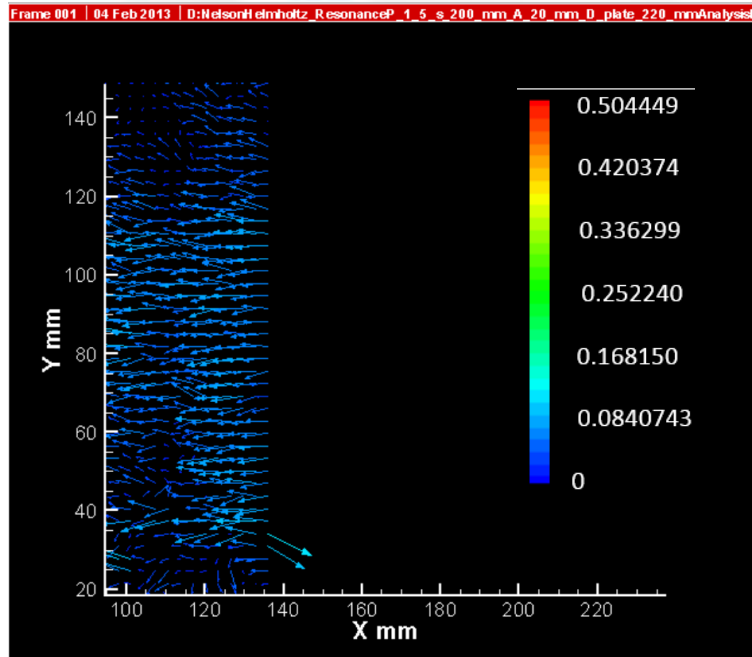


Figure 4-5: Velocity vectors after 1/2 sec.

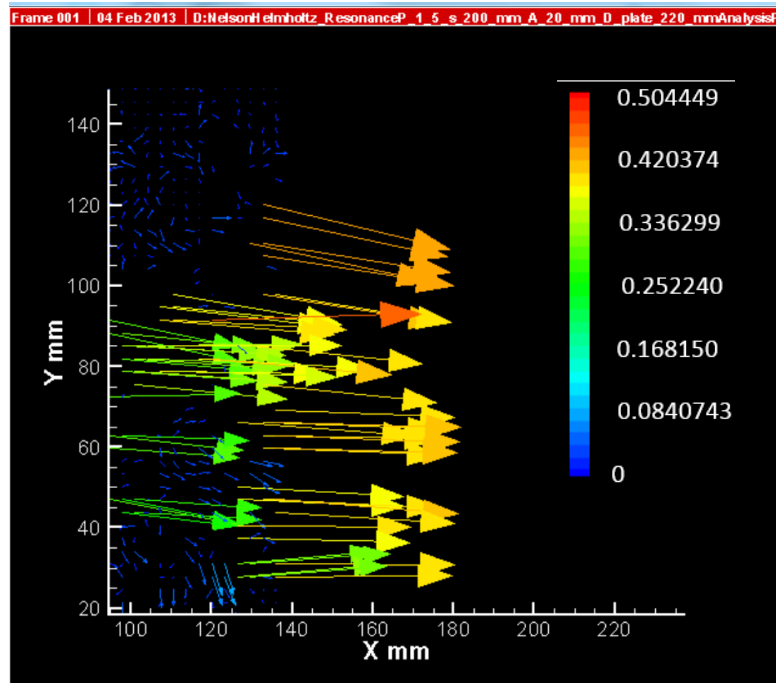


Figure 4-6: Velocity vectors after 2/3 sec.

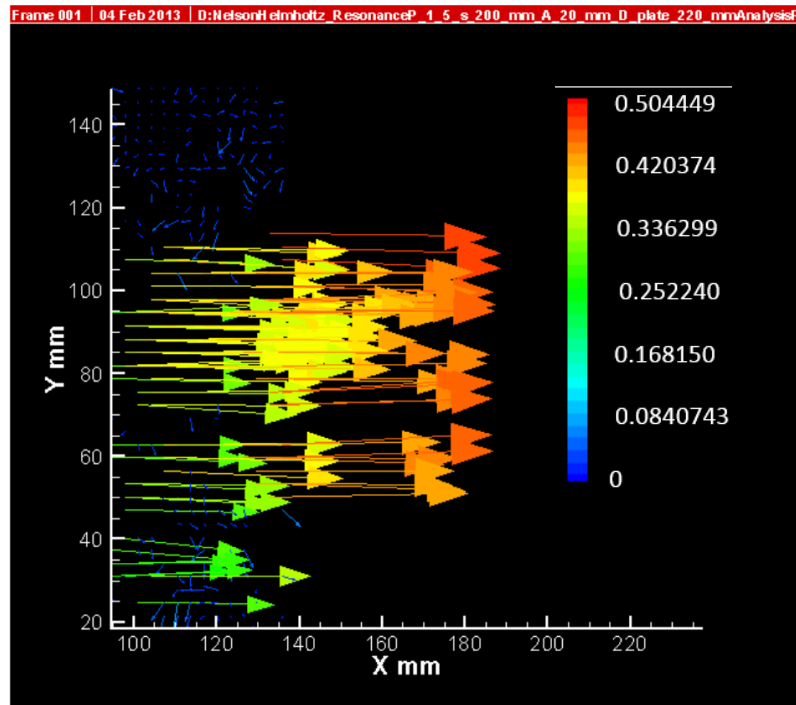


Figure 4-7: Velocity vectors after 5/6 sec.

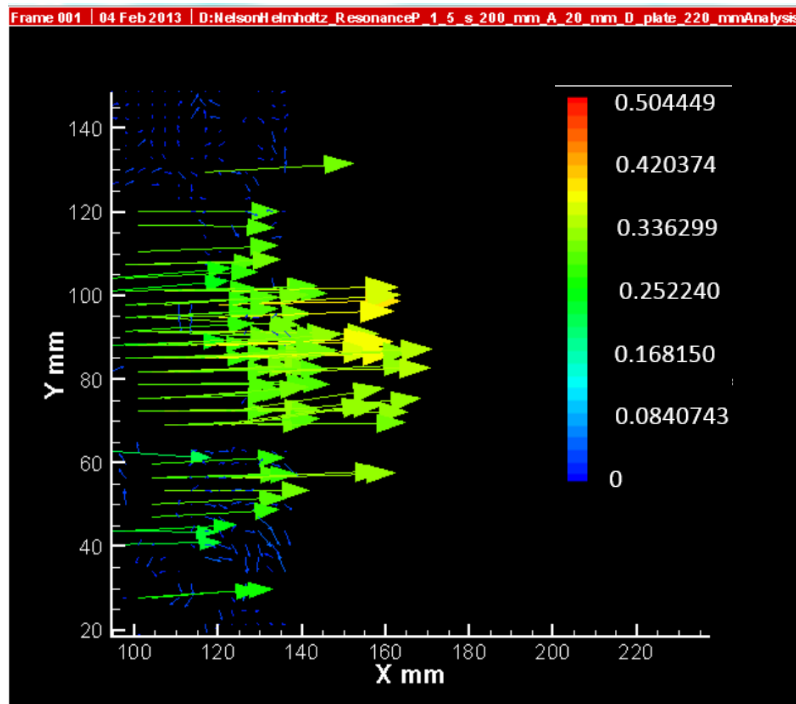


Figure 4-8: Velocity vectors after 1 sec.

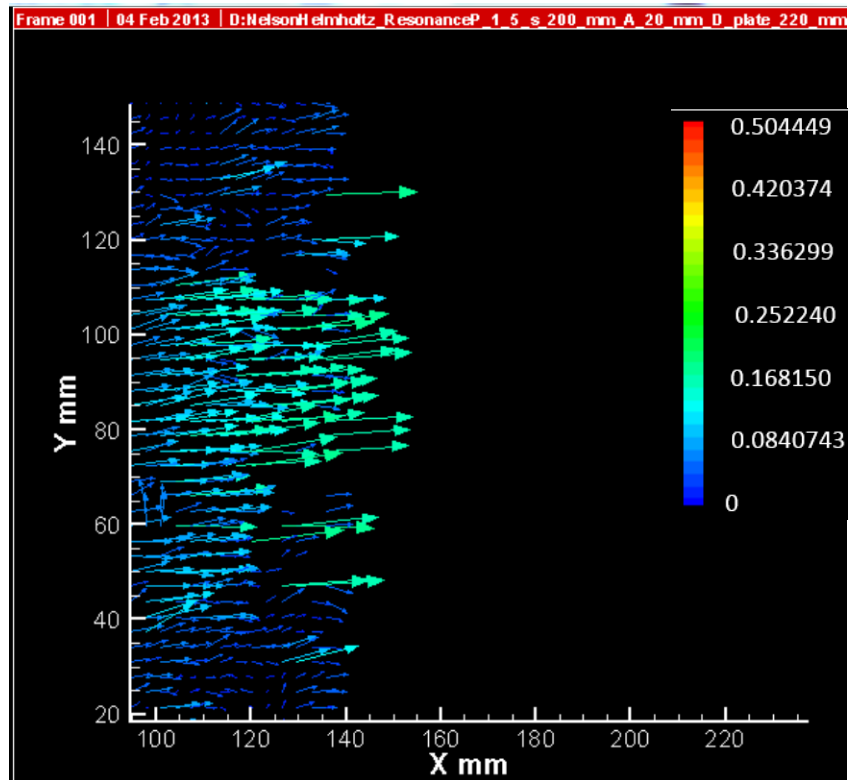


Figure 4-9: Velocity vectors after 1 1/2 sec.

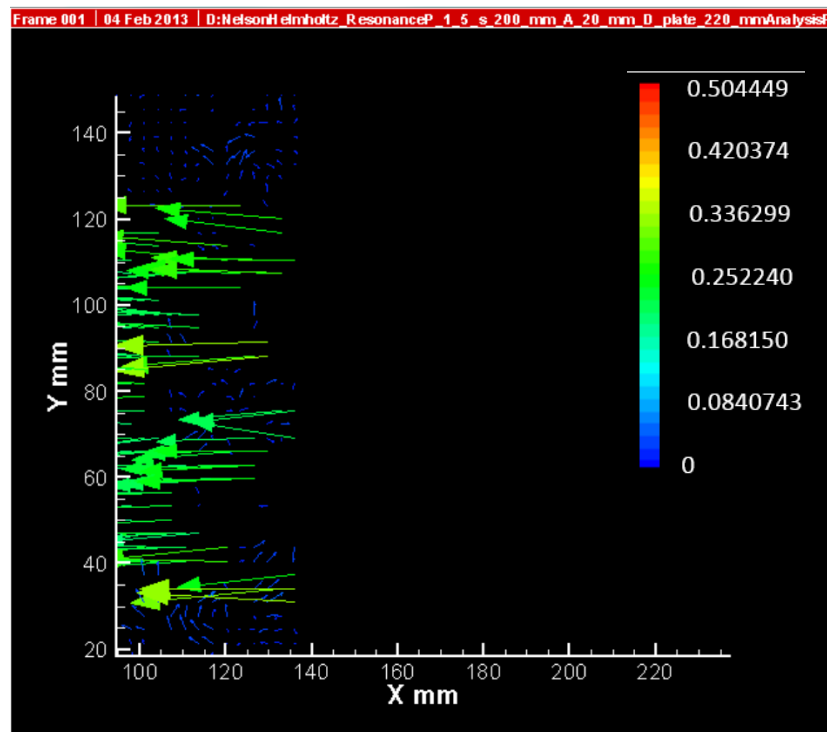


Figure 4-10: Velocity vectors after 1 1/3 sec.

It may be observed that the direction of the velocity vectors reverses between $\frac{1}{2}$ seconds and $\frac{2}{3}$ seconds, and again between $1\frac{1}{3}$ seconds and $1\frac{1}{2}$ seconds, at the instances when average velocity is zero. Maximum velocity is seen to occur at $\frac{5}{6}$ seconds with a magnitude of 0.48 m/s, occurring exactly at a time equal to $T/2$, and at a distance of 0.1 meters from the water surface.

Additionally, the maximum magnitude of average velocity occurred at the same time, with a value of 0.19 m/s. The curves for maximum and minimum (maximum outflow) particle velocities over time, plotted along with the curve for average velocity in the channel over time, are shown in Fig. 4-11. These curves are obtained from curve fitting of data with a 6th degree polynomial trend line with acceptable error of 5%.

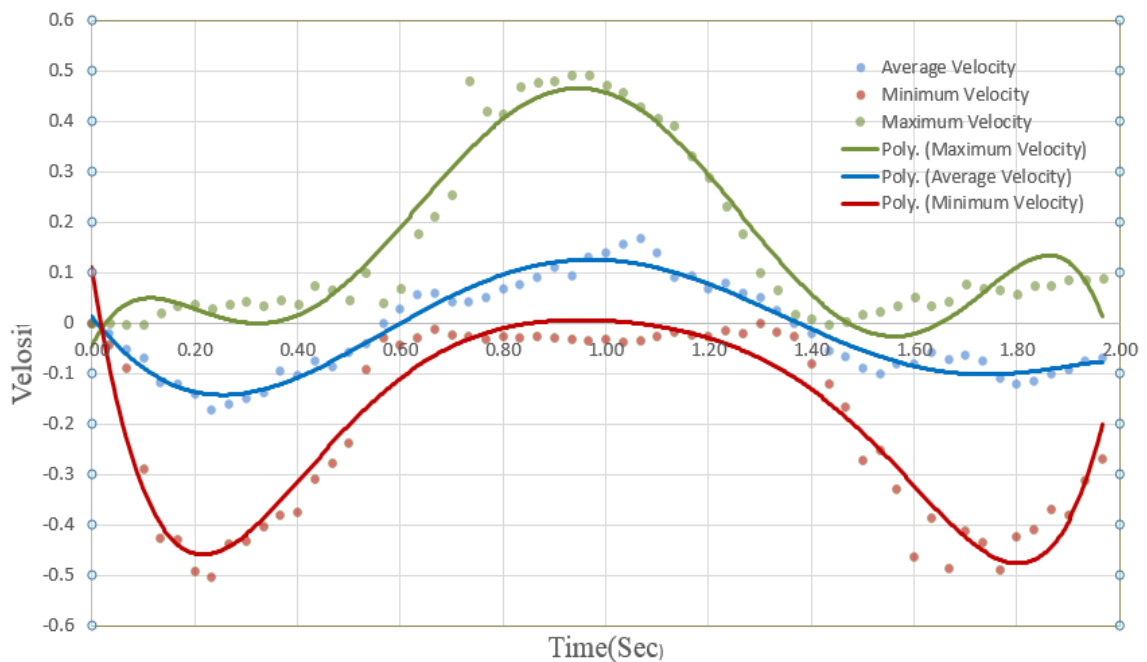


Figure 4-11: Average velocity (m/s) in whole channel, maximum, and minimum particle velocity at each instantaneous time in the channel

Figure 4-11 also illustrates the result that, when the system approaches Helmholtz resonance, the three velocities follow expected behavior such that their peak values coincide at the appropriate time. However, when the system is not at resonance, the three velocity measures do not agree, as made evident by an inconsistent plot of standard deviations. In this case, the average velocity does indeed show the entire water mass oscillating back and forth, in addition, the particles' maximum and minimum velocities are in the same frequency as the average velocity. Experimenting with the Helmholtz resonance basin has illustrated a means of increasing magnitude of average velocity of the system, corresponding to an increase in available power to be extracted.

CHAPTER 5: SUMMARY AND CONCLUSIONS

The application of the theory of Helmholtz resonance used for wind-driven ocean waves was explored in both 1/25th and 1/7th scale experiments, and in both cases, the theory was successfully validated. The 1/25th scale device was tested with a two-dimensional Particle Image Velocimetry instrument (PIV) to determine the instantaneous velocity field through the scaled model. The first two PIV experiments demonstrated the sensitivity of the device to the channel's width and the basin area. The area of the basin had to be adjusted to match the Helmholtz resonance of its geometry to the incoming wave frequency. Channel width was reduced through the employment of winglets, with the winglet angle affecting the performance of the device such that for angles above 30 degrees, the performance of the device declined, causing flow to change abruptly and leading to larger amplitude of reflected waves at the face of the channel, thereby reducing wave energy transmitted to the basin. It was also found that curved winglets allowed for a much more efficient device with lower energy dissipation.

Channel blockages of 40%, 60% and 80% yielded expected results whereby the lowest blockage had the smallest effect on flow velocity and caused the lowest magnitude of reflected waves, suggesting highest performance gains when a turbine is implemented and the channel is partially blocked.

Resonance in the channel resulted in an amplification of wave height in the basin relative to incoming waves, and thus a corresponding amplification of power within the basin. This suggests that the power take-off (PTO) should be engaged in the part of the channel where the system isn't saturated, rather than where the ratio of amplified waves in the basin to incoming waves is no longer increasing.

Three different angles of attack, $\beta = 0^\circ, 15^\circ, 30^\circ$ as measured between the WEC axis and incoming wave direction of travel were tested, with the ideal power ratio found to occur at $\beta = 0^\circ$, as expected. The power ratio in this case is 4.5, which is 1.6 times greater than $\beta = 15^\circ$ and 3.75 times greater than $\beta = 30^\circ$. Thus, the basin must be placed with the WEC axis parallel to the incoming waves for best performance.

The last experiment that utilized the two-dimensional Particle Image Velocimetry instrument (PIV) was carried out with the following results: The average velocity was plotted along with the maximum and minimum particle velocities over time. The instant of maximum average velocity, and corresponding maximum current and maximum power, were compared to the instants when maximum and minimum particle velocities peak. An analysis of all collected data indicated that the location of maximum velocity occurred at the middle height of the channel, suggesting an ideal location for PTO placement.

CHAPTER 6: REFERENCES

[[1] Masuda, Y., 1972, "Study of Wave Activated Generator and Future View as an Island Power Sources," 2nd International Ocean Development Conference.

[2] Salter, S.H., 1974, "Wave Power," *Nature*., 249:720-723.

[3] Mei, C.C., 1976, "Power Extraction from Water Waves," *Journal of Ship Research*., 20(2):63-66.

[4] Mei, C.C., and Newman, J.N., 1979, "Wave Power Extraction by Floating Bodies," *Symposium on Ocean Wave Energy Utilization*., 1-28.

[5] Mei, C.C., 1989," *The Applied Dynamics of Ocean Surface Waves*," World Scientific.

[6] Falnes, J., and Budal, K., 1978, "Wave-Power Conversion by Point Absorbers," *Norwegian Maritime Research*., 6(4):2-11.

[7] Falnes, J., 2007, "A Review of Wave Energy Extraction," *Marines Structures*., 20:185-201.

[8] Newman, J.N., 1977, *Marine Hydrodynamics*, M.I.T, Press.

[9] Newman, J.N., and Mei, C.C., 1979, "Wave Power Extraction by Floating Bodies," *Symposium on Ocean Wave Energy Utilization*., 1-28.

[10] Budal, K., and Falnes, J., 1978, "Wave-Power Conversion by Point Absorbers," *Norwegian Maritime Research*., 6(4):2-11.

[11] Evans, D.V., 1976,"A Theory for Wave-Power Absorption by Oscillating Bodies," *Journal of Fluid Mechanics*., 77(1):1-25.

[12] Evans, D.V., 1979, "Some Theoretical Aspects of Three-Dimensional Wave-Energy Absorbers," *Symposium on Ocean Wave Energy Utilization*., 78-112.

[13] Fujita, R.M., and Pelc, R., 2002, "Renewable Energy from the Ocean," Marine Policy., 26:471-479.

[14] Drew, B., Plummer, A.R., and Sahinkaya, M.N., 2009, "A Review of Wave-Energy Converter Technology," Journal of Power and Energy., 223:887-902.

[15] Yemm, R.9. (2008)."Full-scale WECs: Pelamis in Ocean Wave Energy" (J. Cruz, ed.), pp. 304.321.

[16] Aquamarine Power. Available from <http://www.aquamarinepower.com/> (access date April 2013).

[17] Wave power project- Lysekil Available from http://www.el.angstrom.uu.se/forskningsprojekt/WavePower/Lysekilsprojektet_E.html (access date April 2013)

[18] Salter, S.H. (1974). "Wave Power." Nature 249:720-723.

[19] Wachter, A. Neilsen, K. (2010). "Mathematical and Numerical Modeling of the AquaBuOY Wave Energy Converter". Volume 2, pp. 16-33.

[20] Limpet, http://www.wavegen.co.uk/what_we_offer_limpet.htm (access date April 2013)

[21] (WA 2013) Wave Dragon. Available from <http://tinyurl.com/wavegen1/> (access date April 2013).

[22] A. A.E. Price. New Perspectives on Wave Energy Converter Control, PhD thesis, University of Edinburgh, 2009.

[23] T. W. Thorpe, .The wave energy program in the UK and the European Wave Energy Network,. in 4th European Wave Energy Conference, (Denmark), 2000.

[24] G. Thomas, .The theory behind the conversion of ocean wave energy: A review, in
Ocean Wave Energy (J. Cruz, ed.), pp. 41-91, Springer, 2008.

[25] M. J. French, Conceptual design for engineers. London: Design Council, 1975.

[26] S. H. Salter, J. R. M. Taylor, and N. J. Caldwell, Power conversion mechanisms for wave energy, Proceedings of the Institution of Mechanical Engineers, Part M: Journal of Engineering for the Maritime Environment, vol. 216, pp. 1-27, January 2002.

[27] Evans, D.V. 1978, "The Oscillating Water Column Wave-Energy Device," J. Inst. Math Applies 22,423-433.

[28] Doelman, A., and Koendrink, A., and Maas, L.R.M., 2002,"Quasi-periodically forced nonlinear Helmholtz Oscillators," Physica D: Nonlinear Phenomena., 164 (1-2), pp.1-27.

[29] Maas, L.R.M., 1997, "On the nonlinear Helmholtz response of almost-enclosed tidal basins with sloping bottoms," J. Fluid Mech., 349, pp. 361-380.

[30] Saadat, Y., Fernandez, N., and Ghorbani, R. 2013, "The Wave Energy Converter Based On Helmholtz Mode, Inspired By nature," 32nd international conference on ocean, offshore and arctic engineering, Nantes, France.

[31] Saadat, Y. Fernandez, N. Samimi, A. Alam, M. Shakeri, M. Ghorbani, R. 2013 "Helmholtz Resonance Mode For Wave energy Extraction," 10th European wave and tidal energy conference, Alaborg, Denmark 2013.